

Exploring Mg²⁺ and Ca²⁺ Conductors Via Solid-State Metathesis Reactions

Titus Masese,^{a,c} Godwill Mbiti Kanyolo,^{a,b} Yoshinobu Miyazaki,^d Shintaro Tachibana,^e Keigo Kubota,^a Naoya Ishida,^a Kohei Tada,^{a,f} Hiroyuki Ozaki,^a Toyoki Okumura,^a Sahori Takeda,^a Sachio Komori,^g Tomoyasu Taniyama,^g Yuki Orikasa,^e and Tomohiro Saito^d

^aResearch Institute of Electrochemical Energy, National Institute of Advanced Industrial Science and Technology (AIST), 1-8-31 Midorigaoka, Ikeda, Osaka 563-8577, Japan. Email: titus.masese@aist.go.jp; gm.kanyolo@aist.go.jp

^bDepartment of Engineering Science, The University of Electro-Communications, 1-5-1 Chofugaoka, Chofu, Tokyo 182-8585, Japan.

^cAIST-Kyoto University Chemical Energy Materials Open Innovation Laboratory (ChEM-OIL), Sakyo-ku, Kyoto 606-8501, Japan.

^dTsukuba Laboratory, Sumika Chemical Analysis Service (SCAS), Ltd., Tsukuba, Ibaraki 300-3266, Japan.

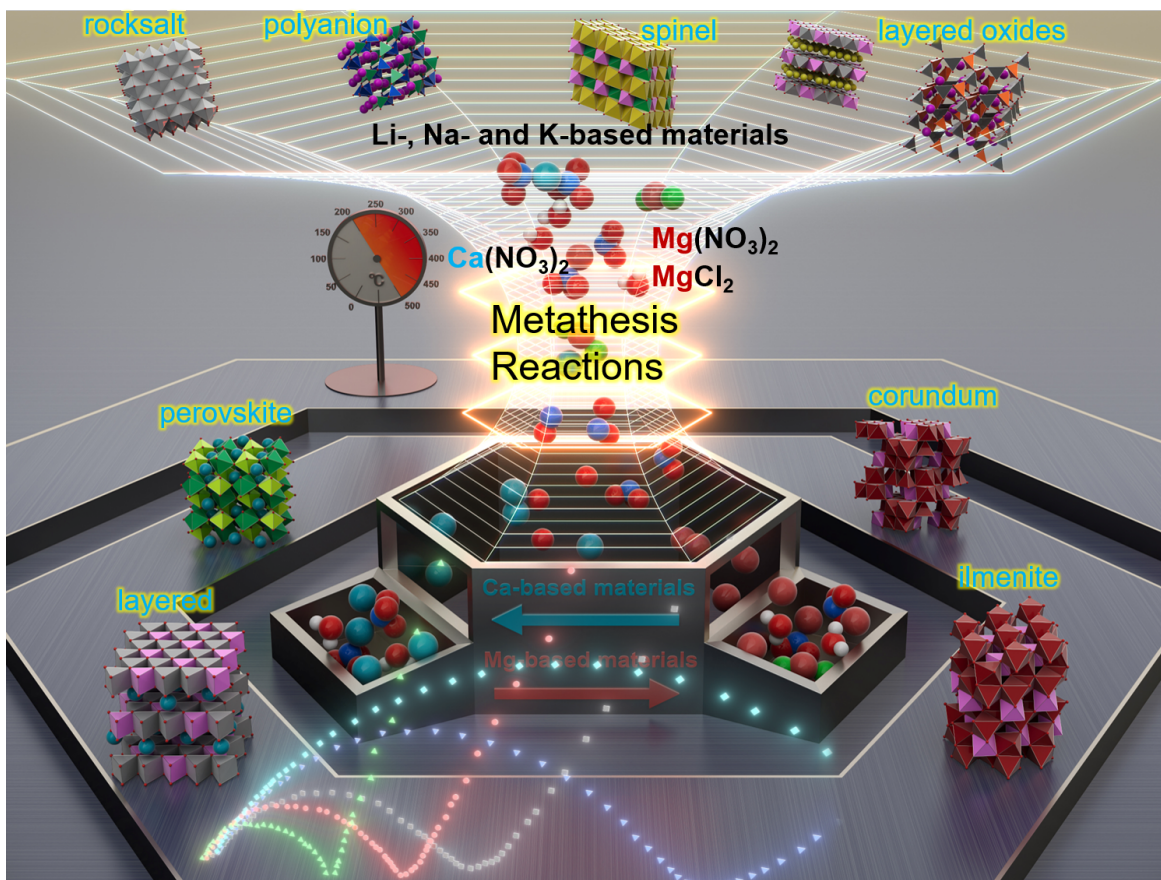
^eGraduate School of Life Sciences, Ritsumeikan University, 1-1-1 Noji-higashi, Kusatsu, Shiga 525-8577, Japan.

^fDepartment of Materials Engineering Science, Graduate School of Engineering Science, Osaka University, 1-3 Machikaneyama-cho, Toyonaka, Osaka 560-8531, Japan.

^gDepartment of Physics, Nagoya University, Furo-cho, Chikusa-ku, Nagoya 464-8602, Japan.

Magnesium and calcium batteries offer promising energy storage solutions characterised by cost-effectiveness, safety, and high energy density. However, the scarcity of viable electrode and electrolyte materials vastly hinders their advancement. This study utilises solid-state metathetical reactions involving predominantly chalcogen- and pnictogen-based honeycomb layered oxides with alkaline-earth halides/nitrates to synthesise Mg²⁺- and Ca²⁺-based materials previously achievable only under high-temperature/high-pressure conditions, as well as new metastable materials with unique crystal versatility. Particularly, we employ metathetical reactions involving Li₄MgTeO₆, Na₂Mg₂TeO₆, and Na₄MgTeO₆ with MgCl₂ / MgSO₄ / Mg(NO₃)₂·6H₂O or Ca(NO₃)₂·4H₂O / CaCl₂·2H₂O at temperatures not exceeding 500 °C to produce Mg₃TeO₆ polymorphs, ilmenite-type CaMg₂TeO₆ / Mg₂CaTeO₆, and double perovskite-type Ca₂MgTeO₆. Thus, we demonstrate that these materials, conventionally requiring gigascale pressures or high temperatures (>1000°C) for their proper synthesis, are now readily accessible at ambient pressure and considerably lower temperatures. Meanwhile, despite sub-optimal pellet densities, the synthesised ilmenite-type Mg₃TeO₆ (high-pressure polymorph) and double perovskite-type Ca₂MTeO₆ (M = Mg, Ca, Zn) materials exhibit remarkable bulk ionic conductivity at room temperature, marking them as promising compositional spaces for exploring novel Mg²⁺ and Ca²⁺ conductors. Furthermore, this study extends the applicability of metathetical reactions to attain Mg- or Ca-based antimonates, ruthenates, titanates, phosphates, and silicates, thus opening avenues to novel high-entropy multifunctional nanomaterial platforms with utility in energy storage and beyond.

Keywords: Multivalent batteries; Solid-State Metathesis Reactions; Layered Tellurates; Magnesium; Calcium; Ionic Conductors

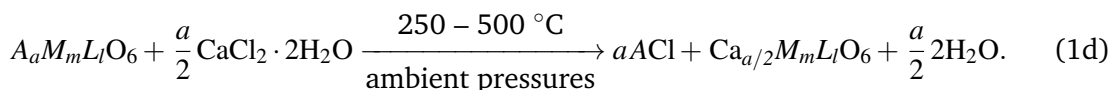
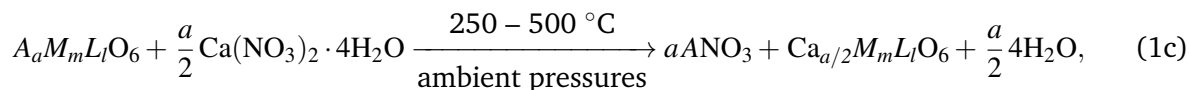
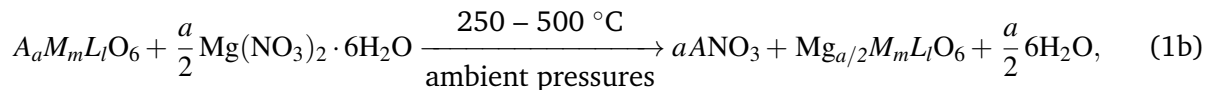
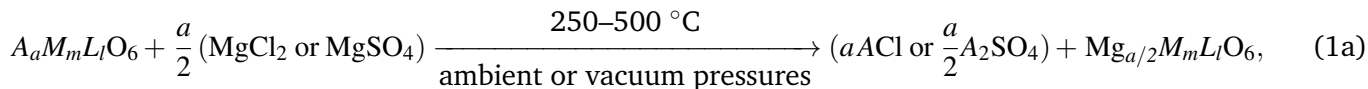


1. Introduction

The dawn of nanotechnology has ushered in a new paradigm of nanomaterials, characterised by a rich tapestry of exceptional chemical properties and physical functionalities. Specifically, honeycomb layered oxides based on pnictogens (group 15 elements) and chalcogens (group 16 elements) have surfaced, showcasing intricate crystal chemistry alongside unique electromagnetic and topological phenomena.^{1–4} These oxide materials hold significant value and elicit diverse interest across multiple disciplines, ranging from condensed matter to materials science, with promising applications in engineering, electronics, and energy storage.^{1,2} This category of layered oxides predominantly encompasses mobile alkali metal cations (such as K, Na, Li) or coinage metal cations (such as Ag or Cu), interposed between layers of primarily transition metals (Zn, Cu, Ni, Co, Fe, Mn, or Cr) arranged in a honeycomb framework encircling chalcogens (such as Te) or pnictogens (Bi, Sb, or As) coordinated with oxygen atoms, thereby presenting an intriguing compositional space.

The syntheses of calcium- and magnesium-based analogue compositions, for instance, through the conventional solid-state ceramics route, often necessitates high temperatures or pressures to obtain the desired target materials.^{5,6} In certain cases, this approach solely yields impurities or non-equilibrium intermediates. Thus, to extend the compositional breadth of the aforementioned class of materials to encompass those that include mobile alkaline-earth metals for multivalent energy storage systems such as Ca and Mg batteries,^{7,8} judicious synthetic routes become imperative. Particularly, solid-state metathesis (double-ion-exchange) reactions are emerging as highly effective synthetic pathways for diverse technologically significant inorganic materials, including pnictides⁹, silicides¹⁰, carbides¹¹, borides¹⁰, metal halides¹², nitrides¹³, phosphides,¹⁴ chalcogenides^{10,15–17} and oxides^{10,18–23}. These reactions are predominantly instigated by the formation of stoichiometric equivalents of a thermodynamically stable byproduct such as a halide or a nitrate with high

lattice energy,¹⁰ in conjunction with the targeted material. For instance, the solid-state metathetic reaction of the alkaline-earth halides, sulphates or nitrates with honeycomb-layered oxide precursor compositions, $A_aM_mL_lO_6$ ^{1,2} where $A = \text{Li, Na, K, Cu, Ag, etc.}$, $M = s\text{-block metal atoms e.g. Ca, Mg or transition metal atoms (e.g., Ni, Co, Cu, Zn, etc.)}$, $L = \text{chalcogen, pnictogen or transition metal atoms (such as Ru, or W, Ta, Nb, etc. (for disordered (rocksalt) derivatives))}$ and $0 < a \leq 4$, $0 < m \leq 2$, $0 < l \leq 1$, can take the form:



The substantial lattice energy of the halide or nitrate coproduct salt (ACl or ANO₃) can rationalise its pivotal role in propelling the reaction forward,^{10,11,16} thereby facilitating the formation of the desired product. Whilst select metathesis reactions may exhibit spontaneous initiation,¹⁰ the majority necessitate additional energy (accomplished via an external heat source or application of microwave electromagnetic radiation) to surmount a sufficient reaction energy barrier, crucial for propagating a synthesis wave.^{10,11,16} Solid-state metathesis reactions then proceed expeditiously, harnessing the liberated enthalpy to elevate the temperature of the precursors, typically surpassing the boiling point of the alkali metal or alkaline-earth metal halide/nitrate. The resulting products, obtained upon completion of the reaction, are readily isolated by trituration with appropriate solvents (such as distilled water, ethanol, methanol, etc.), effectively eliminating the halide/nitrate salts and other metathesis byproducts. Consequently, synthesis through solid-state metathesis reactions offers a straightforward and highly scalable low-temperature methodology to access both new and pre-existing functional materials, otherwise achievable solely at high temperatures.¹⁰ Moreover, the resultant products exhibit distinctive and meticulously controlled nanomorphology.^{15,18,19,24-27}

In this study, we demonstrate that solid-state metathesis reactions involving the broad class of chalcogen- and pnictogen-based honeycomb layered oxides and appropriate alkaline-earth metal chloride/nitrates (as exemplified in equation (1)) is a convenient route to synthesise not only pre-existing materials (attainable only at *high temperatures* or *pressures*), but also new Ca- and Mg-based functional materials at conventionally lower temperatures and ambient pressure (**Supplementary Figure 1**). Solid-state metathesis reaction of, for instance, layered Na₄MgTeO₆ and Na₂Mg₂TeO₆ with Ca(NO₃)₂ · 4H₂O / CaCl₂ · 2H₂O or MgCl₂ / Mg(NO₃)₂ · 6H₂O at low temperatures of 250 – 500 °C yields not only double perovskite-type Ca₂MgTeO₆ and ilmenite-type Mg₃TeO₆ polymorphs that were conventionally only attainable at high temperatures and/or *high pressures* of >1100°C and >10 GPa respectively,^{5,28} but also new metastable phases with unique nanocrystal morphology. Despite their sub-optimal pellet density, electrochemical impedance tests reveal Mg₂CaTeO₆ and the high-pressure Mg₃TeO₆ polymorph materials to show remarkable Mg²⁺ conductivity at room temperature (with an activation energy of 0.47 eV noted for the high-pressure Mg₃TeO₆ polymorph), thus enlisting a new oxide class of Mg²⁺ conductors. Thus, the crowning achievement of our study is successfully extending the solid-state metathesis reaction to the synthesis of a diverse class of new Ca- and Mg-containing layered- and perovskite-based high-entropy multifunctional energy materials.

2. Results

Magnesium- and calcium-based materials were synthesised via solid-state metathesis reactions, utilising target precursors (**Supplementary Figures 2–6**) with Mg and Ca salts (**Supplementary Figures 7–12**), with the reactions performed at temperatures below 500 °C, as detailed in the **Methods** section. The composition of the attained materials were ascertained via energy-dispersive X-ray spectroscopy (**Supplementary Figures 13–40**) or inductively-coupled plasma mass spectrometry (**Supplementary Table 1**). Moreover, the purity and crystallinity of the samples prepared via metathesis reactions were verified using X-ray diffraction (XRD) analyses (**Supplementary Figures 7–12**), as described in the **Methods** section. The XRD patterns predominantly displayed broad and asymmetric Bragg peaks, a characteristic feature of materials synthesised via metathesis routes. This broadening presents challenges in obtaining detailed atomic structural information, likely due to the reduced crystallinity and inherent disorder of the resulting materials. To glean insights into the structure of the materials obtained through solid-state metathetical reactions, particularly regarding the atomic arrangement, we conducted atomic-resolution imaging of the acquired materials along various zone axes. Details regarding sample preparation, measurement protocols, and considerations are elucidated in the **Methods** section.

Figures 1a,b,c,d,e,f present high-resolution scanning transmission electron microscopy (STEM) images of Mg₃TeO₆, obtained via a solid-state metathetic reaction involving Mg halide salt with layered Na₄MgTeO₆ at 400 °C for 99 hours in air (hypothetically, Na₄MgTeO₆ + 2MgCl₂ → Mg₃TeO₆ + 4NaCl). The determined lattice parameters ($a = 5.06 \text{ \AA}$, $c = 13.8 \text{ \AA}$) closely align with those of the ilmenite-type Mg₃TeO₆ polymorph,⁵ typically achieved under high-pressure (12.5 GPa) and high-temperature (1297 °C) conditions, crystallising in the non-centrosymmetric (acentric) *R3* trigonal space group (hereafter referred to as ‘high-pressure, high-temperature Mg₃TeO₆’). Notably, whilst another Mg₃TeO₆ polymorph²⁹ can be obtained via solid-state reaction of Li₄MgTeO₆ and Mg halide salts (**Figures 1g,h,i,j,k,l,m,n,o** and **Supplementary Figure 9**) or using solid-state ceramics route under ambient pressure at high temperatures (**Supplementary Figure 41**), we obtained a previously unreported Mg₃TeO₆ polymorph by modifying the initial precursor from layered Na₄MgTeO₆ to the honeycomb-layered Na₂Mg₂TeO₆ (**Supplementary Figure 7**). **Figures 2a,b,c,d,e,f,g,h,i,j,k,l** display high-resolution STEM images of this polymorph, acquired through a solid-state metathetic reaction involving Na₂Mg₂TeO₆ with Mg(NO₃)₂·6H₂O salt at 250 °C for 48 hours in N₂ (Na₂Mg₂TeO₆ + Mg(NO₃)₂·6H₂O → Mg₃TeO₆ + 2NaNO₃ + 6H₂O ↑). The measured lattice parameters for this new polymorph (hereafter referred to as vacancy-type Mg₃TeO₆) confirm an orthorhombic lattice ($a = 5.12 \text{ \AA}$, $b = 8.91 \text{ \AA}$, $c = 9.37 \text{ \AA}$), crystallising in the possible space groups: *Cmcm*, *C222*₁ or *Cmc*₂₁. Whilst Na₂Mg₂TeO₆ exhibits a honeycomb arrangement of Mg around Te atoms along the slabs (*i.e.*, within the *ab* plane) following the sequence (along the [100] or equivalently [010] direction) given by –Te – Mg – Mg – Te – Mg – Mg – Te–,³⁰ the metathetic reaction results in the vacancy type Mg₃TeO₆ exhibiting a periodic absence of half of the honeycomb array of Mg (denoted by X) within the slab in the sequence: –Te – Mg – Mg – Te – X – X – Te–. In fact, due to the high ionic charge of +2 for Mg²⁺ relative to that of Na¹⁺, the absent Mg²⁺ ions (X ≡ X(Mg)) in **Figures 2f,i** result from electrostatic ejection from their resident slab into the inter-slab layer.

This ejection thesis becomes apparent in the case of MgZn₂TeO₆, where the absent slab atoms are expected to differ from the inter-slab atoms. In particular, a different solid-state metathetic reaction involving honeycomb-layered Na₂Zn₂TeO₆ with Mg salt at 400 °C for 99 hours in air (Na₂Zn₂TeO₆ + MgCl₂ → MgZn₂TeO₆ + 2NaCl) or Mg(NO₃)₂·6H₂O salt at 250 °C for 48 hours in N₂ (Na₂Zn₂TeO₆ + Mg(NO₃)₂·6H₂O → MgZn₂TeO₆ + 2NaNO₃ + 6H₂O ↑) was performed, resulting in a structure (vacancy-type MgZn₂TeO₆) isotypic to that obtained from the metathetic reaction of Na₂Mg₂TeO₆ with Mg salt. High-resolution STEM images in **Figures 3a,b,c,d,e,f** depict the resulting vacancy-type MgZn₂TeO₆, revealing the periodic absence of half of the Zn atoms in the

honeycomb array within the slab that follows the periodic sequence (along the [100] or equivalently [010] direction): $-Te - Zn - Zn - Te - X - X - Te-$. The absent Zn atoms ($X \equiv X(Zn)$) translocate between the slabs,

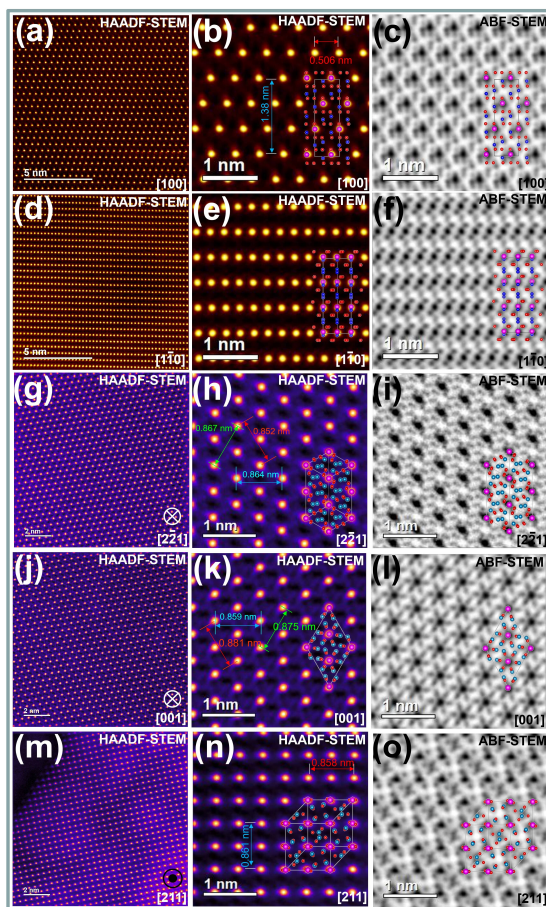


Figure 1 : Visualisation of the crystal structures of high-pressure, high-temperature Mg_3TeO_6 (ilmenite-type) polymorph (prepared via solid-state metathesis reaction of layered Na_4MgTeO_6 precursor with anhydrous $MgCl_2$ at $400^\circ C$ for 99 hours in air. A two-fold molar excess of anhydrous $MgCl_2$ was used.), and ambient-pressure, high-temperature Mg_3TeO_6 (corundum-type) polymorph (prepared via solid-state metathesis reaction of Li_4MgTeO_6 precursor with anhydrous $MgCl_2$ at $400^\circ C$) using high-resolution scanning transmission electron microscopy (STEM). To be visually distinguishable, Mg atoms are shown in (dark/light) blue whilst Te and O atoms are shown in pink and red, respectively. (a) High-angle annular dark-field (HAADF)-STEM image of high-pressure, high-temperature Mg_3TeO_6 polymorph crystallite taken along the [100] zone axis. (b) Enlarged HAADF-STEM image and (c) Corresponding annular bright-field (ABF)-STEM image. (d) HAADF-STEM image of high-pressure, high-temperature Mg_3TeO_6 crystallite taken along the $[1\bar{1}0]$ zone axis. (e) Enlarged HAADF-STEM image and (f) Corresponding ABF-STEM image. An atomistic model of the average structure of high-pressure, high-temperature Mg_3TeO_6 acquired based on STEM analyses along the [100] and $[1\bar{1}0]$ zone axes has been embedded on the STEM images. (g) HAADF-STEM image of ambient-pressure, high-temperature Mg_3TeO_6 polymorph crystallite taken along the [221] zone axis and (h) Corresponding ABF-STEM image. (i) Enlarged ABF-STEM image taken along the [221] zone axis. (j) HAADF-STEM image of ambient-pressure, high-temperature Mg_3TeO_6 polymorph crystallite taken along the [001] zone axis and (k) Corresponding ABF-STEM image. (l) Enlarged ABF-STEM image taken along the [001] zone axis. (m) HAADF-STEM image of ambient-pressure, high-temperature Mg_3TeO_6 polymorph crystallite taken along the [211] zone axis and (n) Corresponding ABF-STEM image. (o) Enlarged ABF-STEM image taken along the [211] zone axis. An atomistic model of the average structure of ambient-pressure, high-temperature Mg_3TeO_6 polymorph acquired based on STEM analyses along the [221], [001] and [211] zone axes has been embedded on the STEM images.

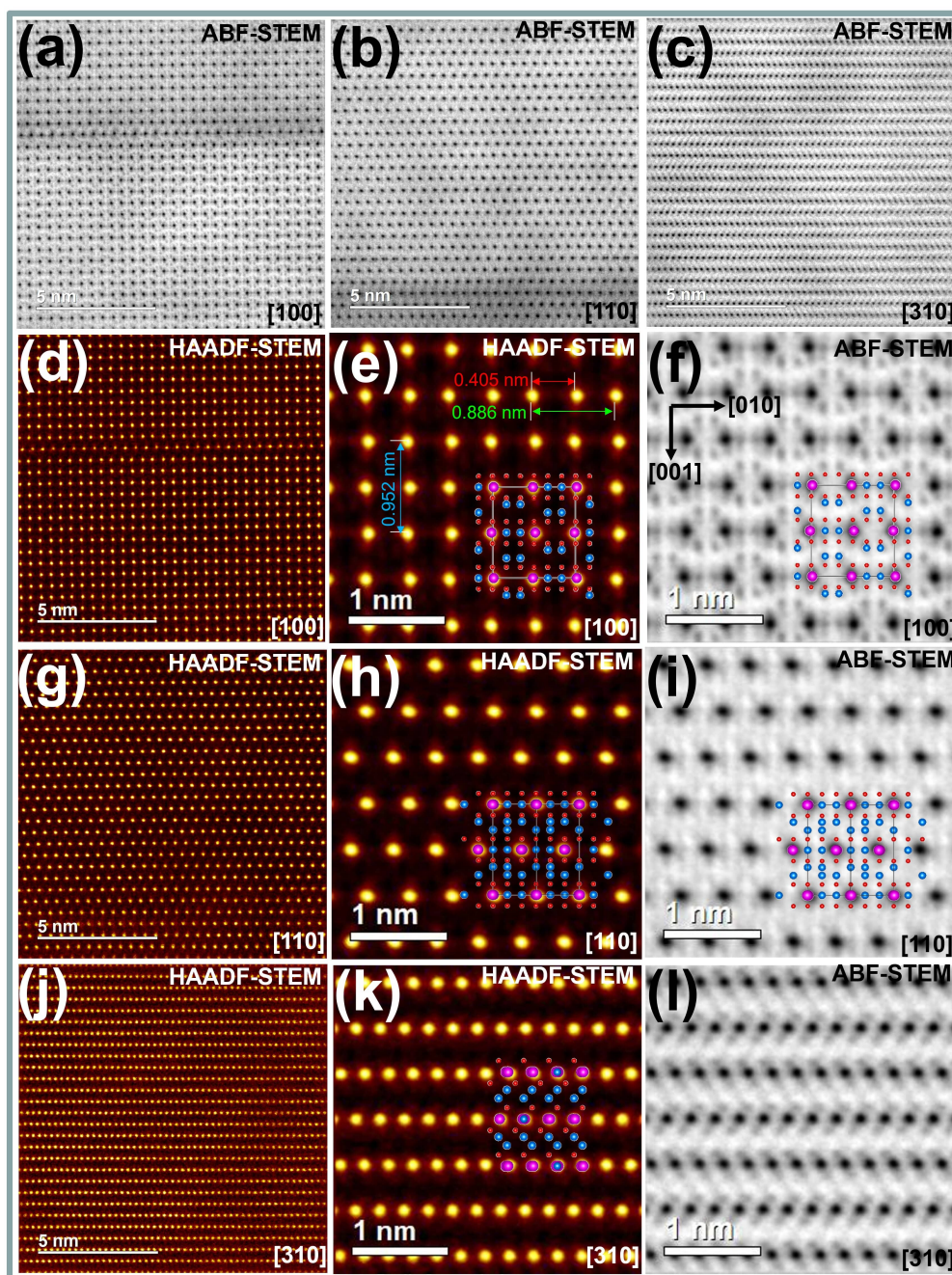


Figure 2 : Visualisation of the crystal structure of vacancy-type Mg_3TeO_6 (prepared via solid-state metathesis reaction of honeycomb-layered $\text{Na}_2\text{Mg}_2\text{TeO}_6$ precursor with $\text{Mg}(\text{NO}_3)_2 \cdot 6\text{H}_2\text{O}$ at 250°C for 48 hours in N_2 under ambient pressure) using high-resolution STEM. To be visually distinguishable, Mg atoms are shown in (dark/light) blue whilst Te and O atoms are shown in pink and red, respectively. ABF-STEM image of vacancy-type Mg_3TeO_6 (low-temperature polymorph) crystallite taken along (a) [100], (b) [110] and (c) [310] zone axes. (d) HAADF-STEM image of Mg_3TeO_6 crystallite taken along the [100] zone axis. (e) Enlarged HAADF-STEM image and (f) Corresponding ABF-STEM image. (g) HAADF-STEM image of Mg_3TeO_6 crystallite taken along the [110] zone axis. (h) Enlarged HAADF-STEM image and (i) Corresponding ABF-STEM image. (j) HAADF-STEM image of Mg_3TeO_6 crystallite taken along the [310] zone axis. (k) Enlarged HAADF-STEM image and (l) Corresponding ABF-STEM image. An atomistic model of the average structure of Mg_3TeO_6 acquired based on STEM analyses along the [100], [110] and [310] zone axes has been embedded on the STEM images.

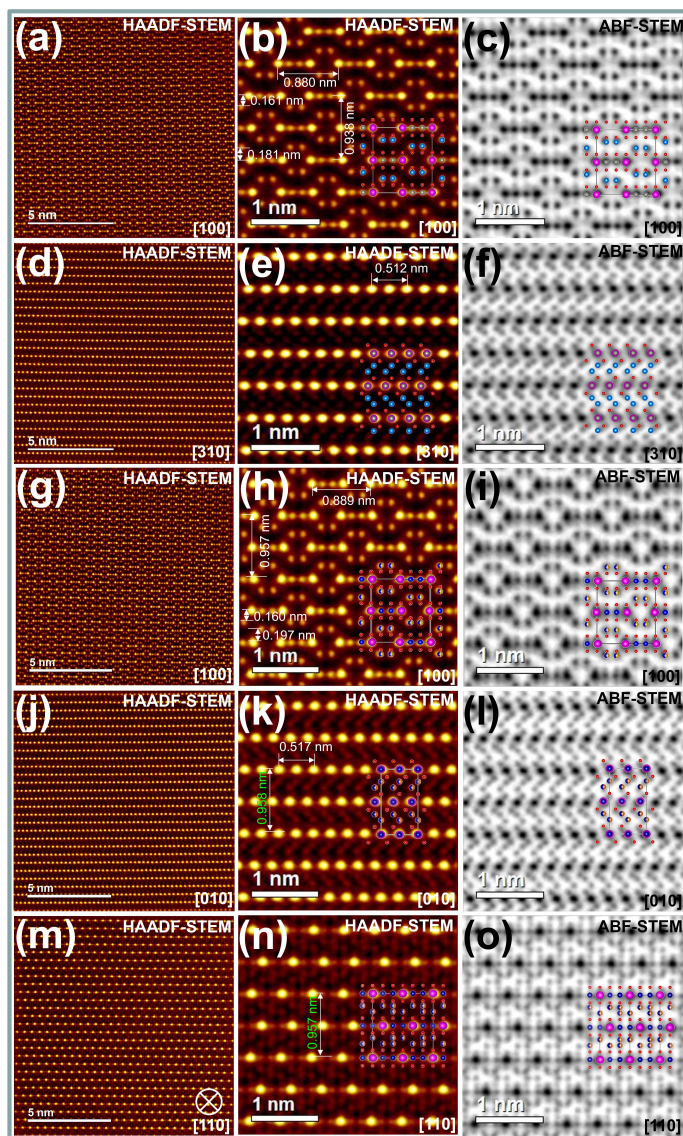


Figure 3 : Visualisation of the crystal structures of vacancy-type $\text{MgZn}_2\text{TeO}_6$ and $\text{MgCo}_2\text{TeO}_6$ (prepared via solid-state metathesis reaction of honeycomb-layered $\text{Na}_2\text{Zn}_2\text{TeO}_6$ and $\text{Na}_2\text{Co}_2\text{TeO}_6$ precursors with $\text{Mg}(\text{NO}_3)_2 \cdot 6\text{H}_2\text{O}$ at 250°C for 48 hours in N_2 under ambient pressure) using high-resolution STEM. (a) HAADF-STEM image of vacancy-type $\text{MgZn}_2\text{TeO}_6$ crystallite taken along the [100] zone axis. (b) Enlarged HAADF-STEM image and (c) Corresponding ABF-STEM image. (d) HAADF-STEM image of $\text{MgZn}_2\text{TeO}_6$ crystallite taken along the [310] zone axis. (e) Enlarged HAADF-STEM image and (f) Corresponding ABF-STEM image. An atomistic model of the average structure of vacancy-type $\text{MgZn}_2\text{TeO}_6$ acquired based on STEM analyses along the [100] and [310] zone axes has been embedded on the STEM images. To be visually distinguishable, Mg atoms are shown in (light) blue whilst Te, Zn and O atoms are shown in pink, grey and red, respectively. (g) HAADF-STEM image of vacancy-type $\text{MgCo}_2\text{TeO}_6$ crystallite taken along the [100] zone axis. (h) Enlarged HAADF-STEM image and (i) Corresponding ABF-STEM image. (j) HAADF-STEM image of $\text{MgCo}_2\text{TeO}_6$ crystallite taken along the [010] zone axis. (k) Enlarged HAADF-STEM image and (l) Corresponding ABF-STEM image. (m) HAADF-STEM image of $\text{MgCo}_2\text{TeO}_6$ crystallite taken along the [110] zone axis. (n) Enlarged HAADF-STEM image and (o) Corresponding ABF-STEM image. Atomistic models of the average structure of $\text{MgCo}_2\text{TeO}_6$ acquired based on STEM analyses along the [100], [010] and [110] zone axes have been embedded on the STEM images. To be visually distinguishable, Mg atoms are shown in (light) brown whilst Te and Co atoms are shown in pink and blue, respectively. Oxygen atoms are shown in red.

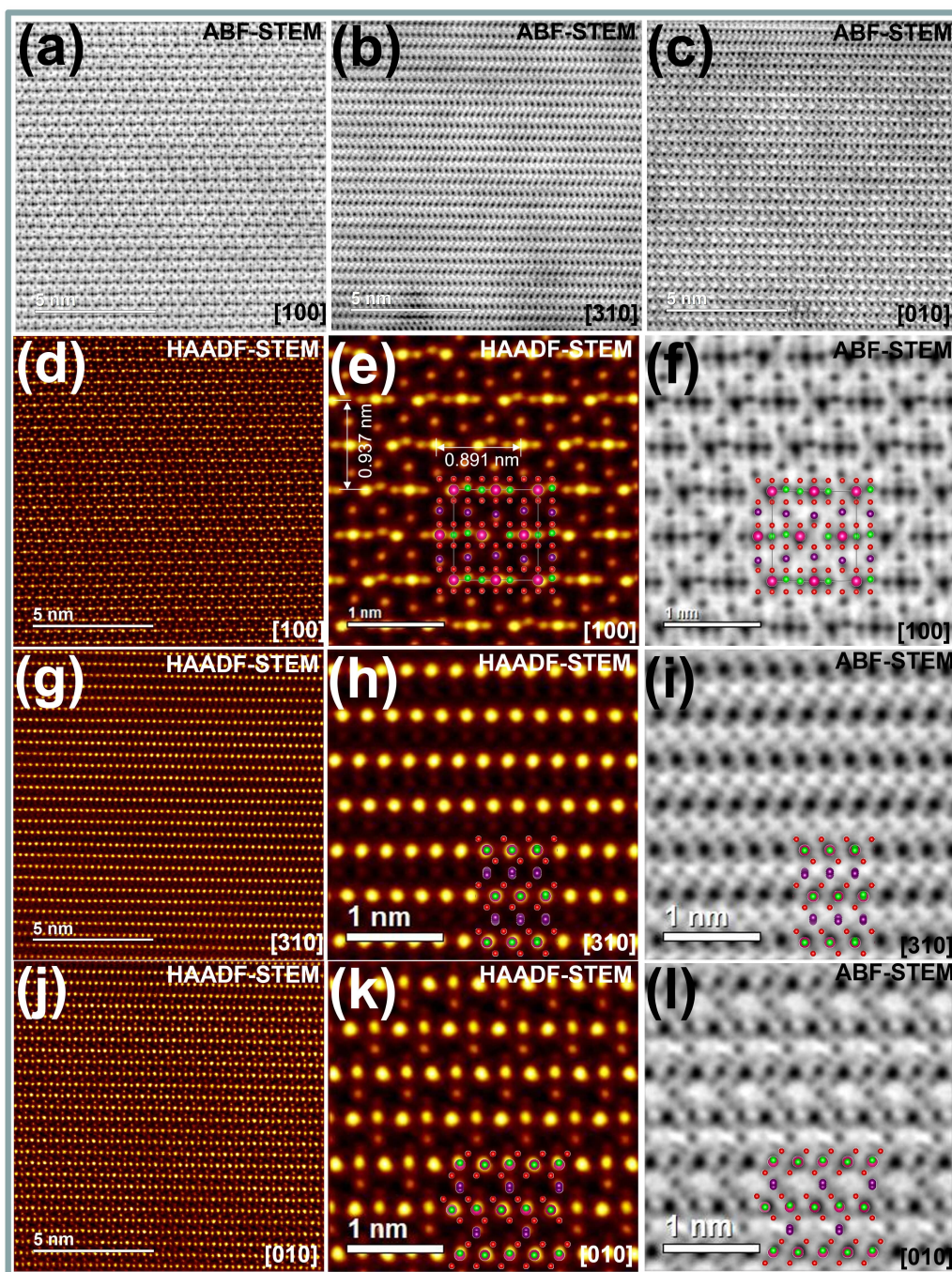


Figure 4 : Visualisation of the crystal structure of $\text{MgNi}_2\text{TeO}_6$ (prepared using solid-state metathesis reaction of honeycomb-layered $\text{Na}_2\text{Ni}_2\text{TeO}_6$ precursor with anhydrous MgCl_2 at 400°C) using high-resolution STEM. To be visually distinguishable, Mg atoms are shown in purple whilst Ni, Te and O atoms are shown in green, pink and red, respectively. (a, b, c) ABF-STEM image of $\text{MgNi}_2\text{TeO}_6$ nanocrystallite taken along [100], [310] and [010] zone axes. (d) HAADF-STEM image of $\text{MgNi}_2\text{TeO}_6$ nanocrystallite taken along [100] zone axis. (e) Enlarged HAADF-STEM image and (f) Corresponding ABF-STEM image. (g) HAADF-STEM image of $\text{MgNi}_2\text{TeO}_6$ nanocrystallite taken along [310] zone axis. (h) Enlarged HAADF-STEM image and (i) Corresponding ABF-STEM. (j) HAADF-STEM image of $\text{MgNi}_2\text{TeO}_6$ crystallite taken along the [010] zone axis. (k) Enlarged HAADF-STEM image and (l) Corresponding ABF-STEM image. An atomistic model of the average structure of $\text{MgNi}_2\text{TeO}_6$ acquired based on STEM analyses along the [100], [310] and [010] zone axes has been embedded on the STEM images.

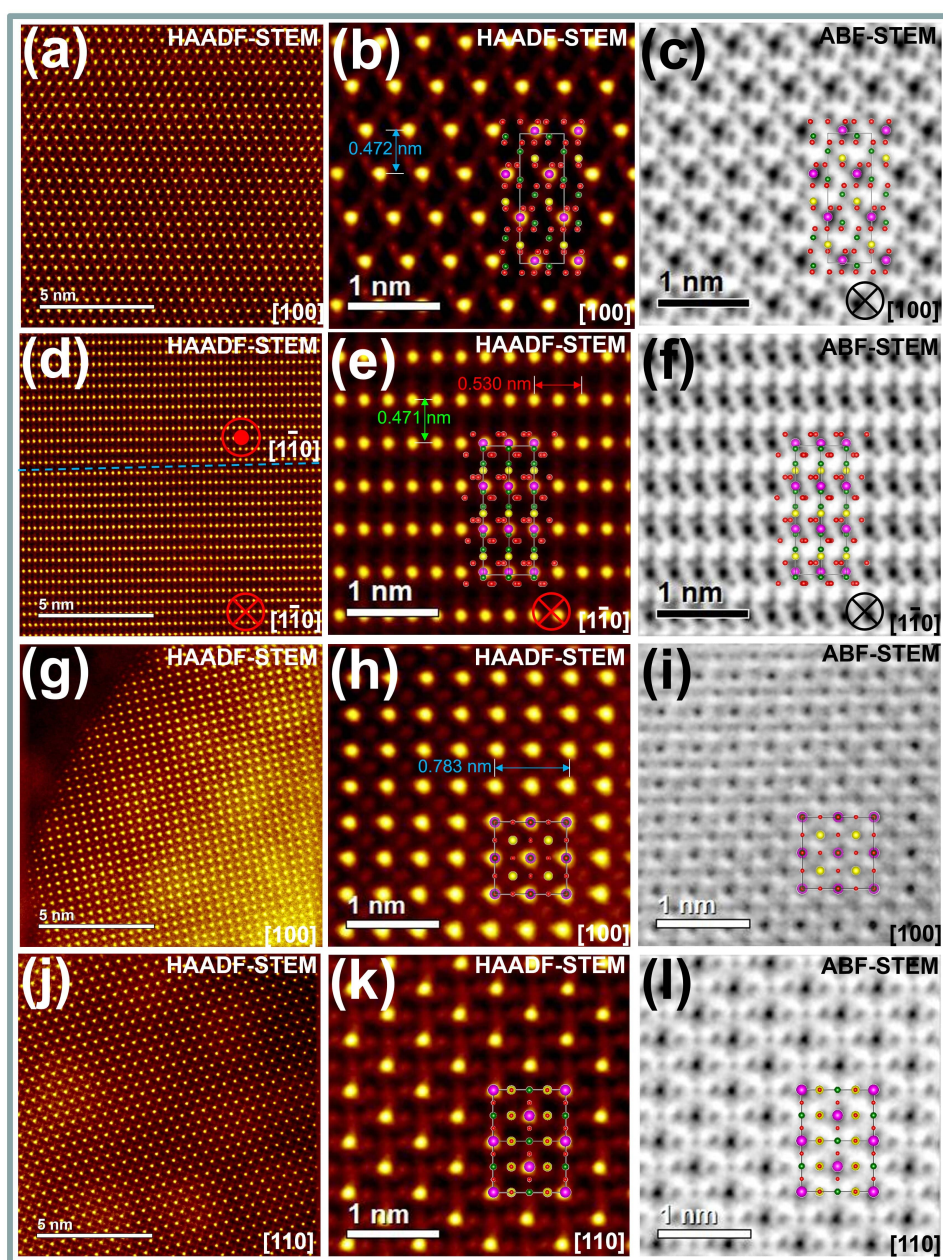


Figure 5 : Visualisation of the crystal structure of $\text{CaMg}_2\text{TeO}_6$ and $\text{Ca}_2\text{MgTeO}_6$ (prepared using solid-state metathesis reaction of honeycomb layered $\text{Na}_2\text{Mg}_2\text{TeO}_6$ and $\text{Na}_4\text{MgTeO}_6$ precursors with $\text{Ca}(\text{NO}_3)_2 \cdot 4\text{H}_2\text{O}$ at 500°C) for 99 hours in N_2 using high-resolution STEM. To be visually distinguishable, Ca atoms are shown in yellow whilst Te, Mg and O atoms are shown in pink, green and red, respectively. (a) HAADF-STEM image of $\text{CaMg}_2\text{TeO}_6$ nanocrystallite taken along the $[100]$ zone axis. (b) Enlarged HAADF-STEM image and (c) Corresponding ABF-STEM image showing the aperiodic structural framework. (d) HAADF-STEM image of $\text{Ca}_2\text{MgTeO}_6$ nanocrystallite taken along the $[1\bar{1}0]$ zone axis. (e) Enlarged HAADF-STEM image and (f) Corresponding ABF-STEM. An atomistic model of the average structure of $\text{CaMg}_2\text{TeO}_6$ acquired based on STEM analyses along the $[100]$ and $[1\bar{1}0]$ zone axes has been embedded on the STEM images. (g) HAADF-STEM image of $\text{Ca}_2\text{MgTeO}_6$ crystallite taken along the $[100]$ zone axis. (h) Enlarged HAADF-STEM image and (i) Corresponding ABF-STEM. (j) HAADF-STEM image of $\text{Ca}_2\text{MgTeO}_6$ crystallite taken along the $[110]$ zone axis. (k) Enlarged HAADF-STEM image and (l) Corresponding ABF-STEM. An atomistic model of the average structure of $\text{Ca}_2\text{MgTeO}_6$ acquired based on STEM analyses along the $[100]$ and $[110]$ zone axes has been embedded on the STEM images.

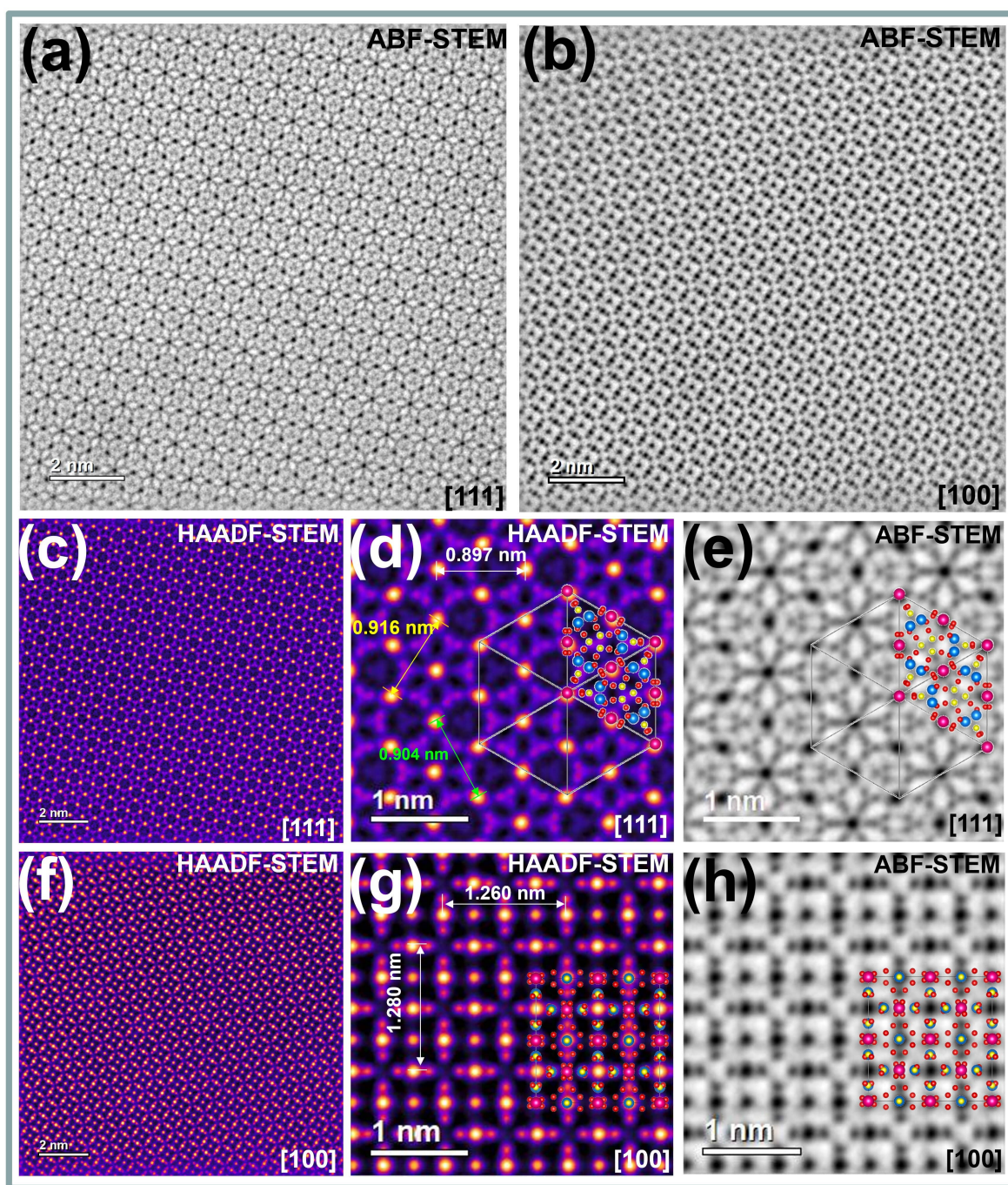


Figure 6 : Visualisation of the crystal structure of $\text{CaZn}_2\text{TeO}_6$ (prepared via solid-state metathesis reaction of honeycomb-layered $\text{Na}_2\text{Zn}_2\text{TeO}_6$ precursor with anhydrous $\text{Ca}(\text{NO}_3)_2 \cdot 4\text{H}_2\text{O}$ at 500°C for 99 hours in N_2) using high-resolution STEM. To be visually distinguishable, Ca atoms are shown in yellow whilst Te, Zn and O atoms are shown in pink, (light)blue and red, respectively. ABF-STEM image of $\text{CaZn}_2\text{TeO}_6$ nanocrystallite taken along the (a) [111] and (b) [100] zone axes. (c) HAADF-STEM image of $\text{CaZn}_2\text{TeO}_6$ nanocrystallite taken along the [111] zone axis. (d) Enlarged HAADF-STEM image and (e) Corresponding ABF-STEM image. (f) HAADF-STEM image of $\text{CaZn}_2\text{TeO}_6$ nanocrystallite taken along the [100] zone axis. (g) Enlarged HAADF-STEM image and (h) Corresponding ABF-STEM image. An atomistic model of the average structure of $\text{CaZn}_2\text{TeO}_6$ acquired based on STEM analyses along the [111] and [100] zone axes has been embedded on the STEM images.

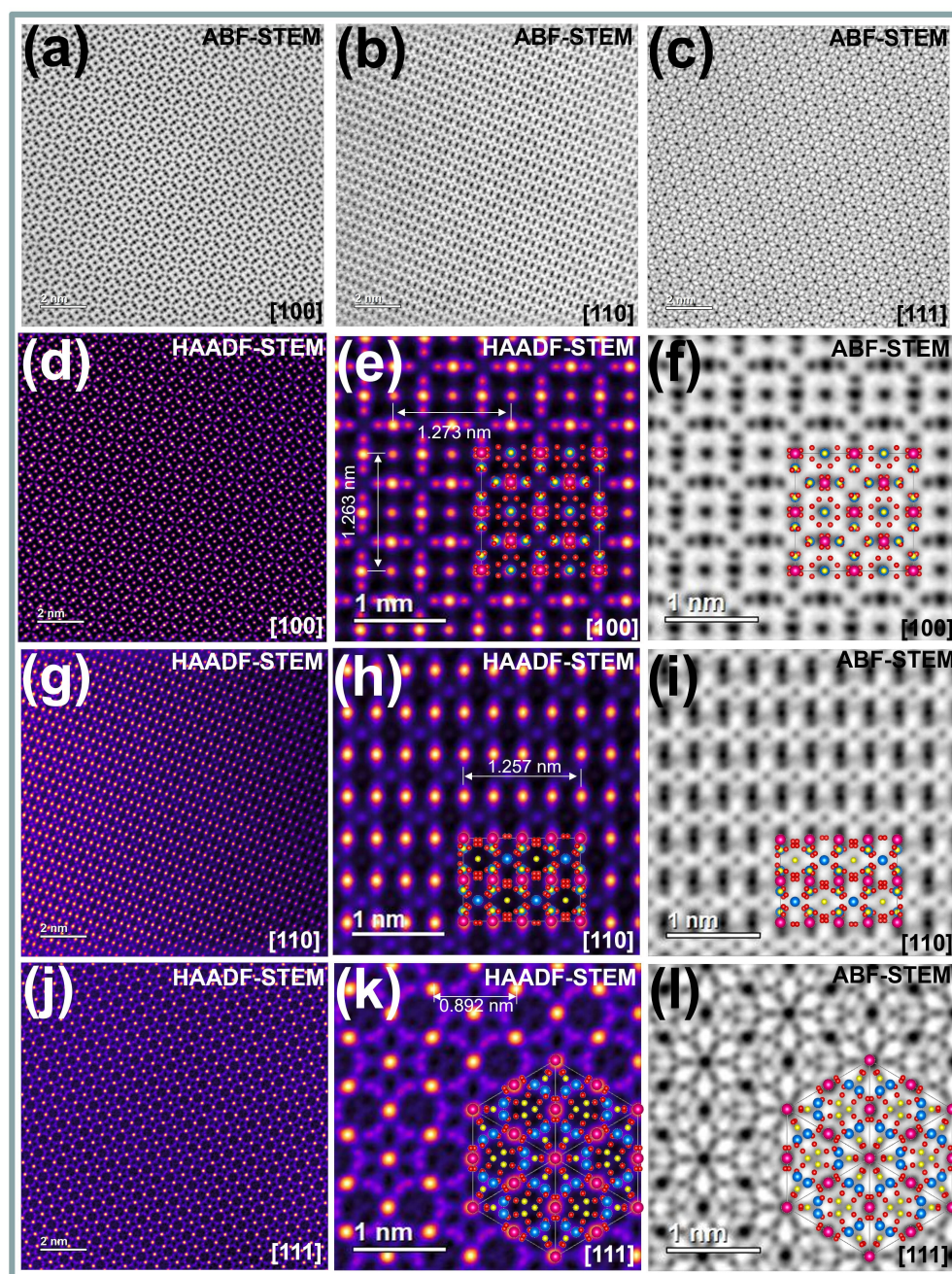


Figure 7 : Visualisation of the crystal structure of yafsoanite-type $\text{Ca}_{1.5}\text{Zn}_{1.5}\text{TeO}_6$ (prepared via metathesis reaction of honeycomb layered $\text{Na}_3\text{Zn}_{1.5}\text{TeO}_6$ precursor with $\text{Ca}(\text{NO}_3)_2 \cdot 4\text{H}_2\text{O}$ at 500°C for 99 hours in nitrogen atmosphere) using high-resolution STEM. To be visually distinguishable, Ca atoms in $\text{Ca}_{1.5}\text{Zn}_{1.5}\text{TeO}_6$ are shown in yellow whilst Te, Zn and O atoms are shown in pink, (light) blue and red, respectively. (a, b, c) ABF-STEM image of $\text{Ca}_{1.5}\text{Zn}_{1.5}\text{TeO}_6$ nanocrystallite taken along [100], [110] and [111] zone axes. (d) HAADF-STEM image of $\text{Ca}_{1.5}\text{Zn}_{1.5}\text{TeO}_6$ crystallite taken along [100] zone axis. (e) Enlarged HAADF-STEM image and (f) Corresponding ABF-STEM image. (g) HAADF-STEM image of $\text{Ca}_{1.5}\text{Zn}_{1.5}\text{TeO}_6$ crystallite taken along [110] zone axis. (h) Enlarged HAADF-STEM image and (i) Corresponding ABF-STEM image. (j) HAADF-STEM image of $\text{Ca}_{1.5}\text{Zn}_{1.5}\text{TeO}_6$ crystallite taken along [111] zone axis. (k) Enlarged HAADF-STEM image and (l) Corresponding ABF-STEM image. An atomistic model of the garnet structure of $\text{Ca}_{1.5}\text{Zn}_{1.5}\text{TeO}_6$ acquired based on STEM analyses along the [100], [110] and [111] zone axes has been embedded on the STEM images.

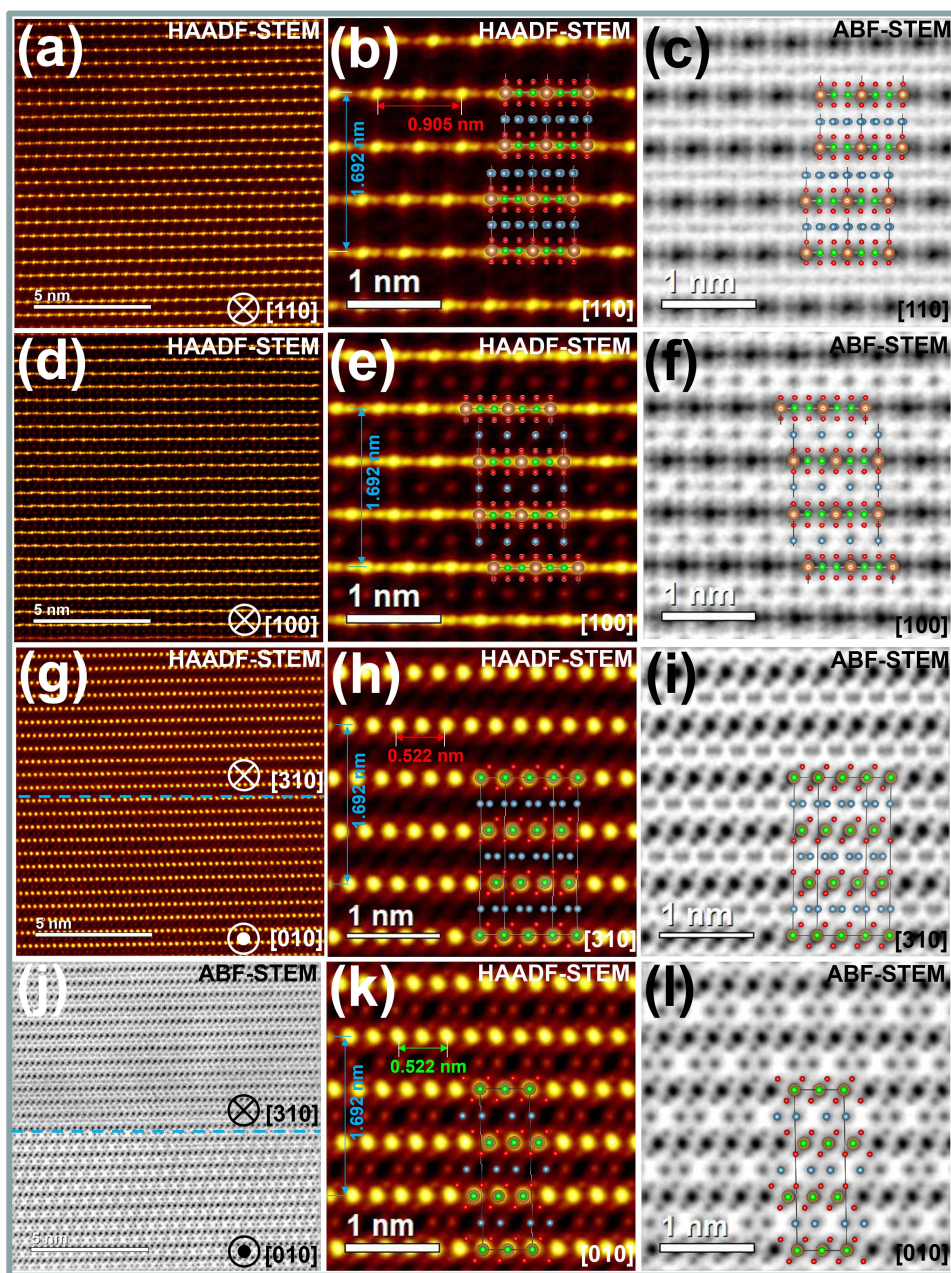


Figure 8 : Visualisation of the crystal structure of honeycomb-layered $\text{Ca}_{1.5}\text{Ni}_2\text{SbO}_6$ (prepared using solid-state metathesis reaction of honeycomb layered $\text{Na}_3\text{Ni}_2\text{SbO}_6$ precursor with $\text{Ca}(\text{NO}_3)_2 \cdot 4\text{H}_2\text{O}$ at 500°C for 99 hours in nitrogen) using high-resolution STEM. To be visually distinguishable, Ca atoms are shown in (light) blue whilst Sb, Ni and O atoms are shown in yellow, green and red, respectively. (a) HAADF-STEM image of $\text{Ca}_{1.5}\text{Ni}_2\text{SbO}_6$ nanocrystallite taken along the [110] zone axis. (b) Enlarged HAADF-STEM image and (c) Corresponding ABF-STEM image showing the aperiodic structural framework. An atomistic model of the average structure of $\text{Ca}_{1.5}\text{Ni}_2\text{SbO}_6$ acquired based on STEM analyses along the [110] zone axis has been embedded on the STEM image. (d) HAADF-STEM image of $\text{Ca}_{1.5}\text{Ni}_2\text{SbO}_6$ nanocrystallite taken along the [100] zone axis. (e) Enlarged HAADF-STEM image and (f) Corresponding ABF-STEM. (g) HAADF-STEM image of $\text{Ca}_{1.5}\text{Ni}_2\text{SbO}_6$ crystallite taken along domains with a juxtaposition of [310] and [010] zone axes. (h) Enlarged HAADF-STEM image taken along the [310] direction and (i) Corresponding ABF-STEM. (j) Low-magnification ABF-STEM image of $\text{Ca}_{1.5}\text{Ni}_2\text{SbO}_6$ crystallite taken along domains with a juxtaposition of [310] and [010] zone axes. (k) Enlarged HAADF-STEM image taken along the [010] direction and (l) Corresponding ABF-STEM.

in near-equal electrostatic competition with Mg in the inter-slab crystallographic sites, as evidenced by their indistinguishable high-angle annular dark-field (HAADF) intensities. These crystallographic sites feature two distinct coordination environments with oxygen ligands: MgO₆ / ZnO₆ octahedral and MgO₄ / ZnO₄ tetrahedral sites (**Supplementary Figures 42 and 43**). The measured lattice parameters for MgZn₂TeO₆ confirm an orthorhombic lattice, ($a = 5.12 \text{ \AA}$, $b = 8.80 \text{ \AA}$, $c = 9.38 \text{ \AA}$) akin to that of the vacancy-type Mg₃TeO₆ (**Figures 2a,b,c,d,e,f,g,h,i,j,k,l**). Likewise, the solid-state metathesis reaction of honeycomb-layered Na₂Co₂TeO₆ with Mg salt at 250 °C yields MgCo₂TeO₆ ($\text{Na}_2\text{Co}_2\text{TeO}_6 + \text{Mg}(\text{NO}_3)_2 \cdot 6\text{H}_2\text{O} \longrightarrow \text{MgCo}_2\text{TeO}_6 + 2\text{NaNO}_3 + 6\text{H}_2\text{O} \uparrow$), adopting a vacancy-type structure analogous to MgZn₂TeO₆ (**Figures 3g,h,i,j,k,l,m,n,o**). The solid-state metathetic reaction of honeycomb-layered Na₂Ni₂TeO₆ with Mg salt at 250 °C yields MgNi₂TeO₆ ($\text{Na}_2\text{Ni}_2\text{TeO}_6 + \text{MgCl}_2 \longrightarrow \text{MgNi}_2\text{TeO}_6 + 2\text{NaCl}$), displaying a unique atomic arrangement (distinct from the Ni₃TeO₆-type MgNi₂TeO₆ structure attainable through high-temperature ceramics route (**Supplementary Figure 41**)) as depicted in **Figures 4a,b,c,d,e,f,g,h,i,j,k,l**. A detailed exposition is provided within the **Methods and Supplementary Information (Supplementary Tables 2–5)** section on the widespread utility of solid-state metathesis reactions, conducted at temperatures not exceeding 400 °C and employing designated precursors with Mg salts such as MgCl₂, MgSO₄, MgSO₄·7H₂O, MgBr₂·6H₂O, MgCl₂·6H₂O, or Mg(NO₃)₂·6H₂O. This versatile approach demonstrates its effectiveness in synthesising various Mg-based compounds, encompassing Mg₂MTeO₆ ($M = \text{Mg, Ca, Ni, Cu, Co, Zn}$), Mg_{1.5}M_{1.5}TeO₆, Mg_{1.5}M₂BiO₆, Mg_{1.5}M₂SbO₆, Mg_{1.5}M₂RuO₆, and other derivatives (**Supplementary Table 1**).

Meanwhile, in **Figures 4e,f**, a periodic absence of 1/4 of the honeycomb array of Ni within the slab is evident. The missing Ni atoms relocate between the intra- and inter-slabs, thus coexisting with Mg, as indicated by the HAADF intensity. In fact, the inter-slab Mg / Ni atoms shift towards the voids (vacancies) in the intra-slabs, resulting in distorted MgO₆ / NiO₆ octahedra (**Supplementary Figure 44**). As a result, there is a one-to-one correlation between the emergent displacement pattern in the inter-slabs and the location on the vacancies in the intra-slabs. **Figures 1b,c**, **Figures 2e,f**, **Figures 3b,c** and **Figures 3h,i** also exhibit this correlation between vacancies and displacements observed in **Figures 4e,f**, corresponding to global wave-like or sawtooth-like patterns (akin to a sawtooth function or castle rim function) across the a, b -axes, stacked in-phase (0°) and/or out-of-phase (180°) along the c -axis (*i.e.*, across the slabs), *albeit* indiscernible at the local level of the unit cell (**Supplementary Figure 45**). This kind of emergence of periodicity is antagonistic to concepts such as aperiodic lattices/tilings (*e.g.* the Einstein problem³¹), whereby locally identical unit cells leads to emergence of global aperiodicity.

In an effort to explore material classes containing calcium, solid-state metathetic reactions were conducted using Ca salt at 500 °C (see **Methods and Supplementary Information** section (**Supplementary Tables 6 and 7**)). The reaction involving honeycomb-layered Na₂Mg₂TeO₆ and Ca(NO₃)₂·4H₂O ($\text{Na}_2\text{Mg}_2\text{TeO}_6 + \text{Ca}(\text{NO}_3)_2 \cdot 4\text{H}_2\text{O} \longrightarrow \text{CaMg}_2\text{TeO}_6 + 2\text{NaNO}_3 + 4\text{H}_2\text{O} \uparrow$) at 500 °C produces a distinctive framework (**Figures 5a,b,c,d,e,f**), where half of the Mg atoms translocate between the (inter/intra-)slabs, resulting in systematically arranged vacancies within the slabs. This arrangement extends to the positions of Ca, Mg, and vacancies between these slabs. The crystal structure of Ca₂MgTeO₆ (or equivalently Mg₂CaTeO₆) mirrors the ilmenite-type Mg₃TeO₆, with measured lattice parameters $a = 5.30 \text{ \AA}$, $c = 14.13 \text{ \AA}$ (acentric space group $R\bar{3}$). Mg₂CaTeO₆ exhibits an expanded unit cell dimension compared to the ilmenite-type Mg₃TeO₆ (**Supplementary Figure 46**), owing to the larger Shannon-Prewitt ionic radius of Ca²⁺ in octahedral coordination with oxygen atoms in comparison to Mg²⁺.³² Moreover, the CaO₆ and MgO₆ octahedra exhibit distortion, with each atom deviating significantly towards the vacancies from the centre. Further, the intricate stacking nature of the slabs is evident in **Figure 5d**, entailing the rotation of Te slabs – a structural disorder that has also been observed in vacancy-type MgNi₂TeO₆ (**Supplementary Figure 47**), vacancy-type MgZn₂TeO₆ (**Supplementary Figure 48**) and honeycomb-layered Na₃Ni₂SbO₆.³³

Furthermore, metathetic reactions, achieved by modifying the initial precursor from Na₂Mg₂TeO₆ to Na₄MgTeO₆, result in calcium-based double perovskite and garnet frameworks. **Figures 5g,h,i,j,k,l** show STEM images of the double perovskite ordered Ca₂MgTeO₆, obtained through the solid-state metathetic reaction of Na₄MgTeO₆ with Ca(NO₃)₂·4H₂O (Na₄MgTeO₆ + 2Ca(NO₃)₂·4H₂O → Ca₂MgTeO₆ + 4NaNO₃ + 8H₂O ↑) at 500 °C. Ca₂MgTeO₆ crystallises in a cubic lattice with lattice constants $a = b = c = 7.83 \text{ \AA}$. However, there is a possibility of lattice distortion leading to the loss of crystal symmetry, as commonly observed in perovskite frameworks (in Glazer notation³⁴: $a^0b^0c^0 \rightarrow a^\pm b^\pm c^\pm$). The reaction involving honeycomb-layered Na₂Zn₂TeO₆ and Ca(NO₃)₂·4H₂O (Na₂Zn₂TeO₆ + Ca(NO₃)₂·4H₂O → CaZn₂TeO₆ + 2NaNO₃ + 4H₂O ↑) at 500 °C yields a garnet framework (**Figures 6a,b,c,d,e,f,g,h**), isotypic to that of yafsoanite-type Ca_{1.5}Zn_{1.5}TeO₆.³⁵ CaZn₂TeO₆ crystallises in a cubic lattice ($Ia\bar{3}d$ space group) with lattice constants $a = b = c = 12.7 \text{ \AA}$.

The universality of solid-state metathetic reactions extends not only to the synthesis of CaM₂TeO₆ ($M = \text{Mg, Ca, Ni, Cu, Co, Zn}$) and Ca₂MTeO₆ compounds but also to the generation of other new compounds, such as those belonging to classes like Ca_{1.5}M_{1.5}TeO₆, Ca_{1.5}M₂RuO₆, CaMSiO₄, honeycomb-layered Ca_{1.5}M₂SbO₆, Ca_{1.5}M₂BiO₆, etc., as detailed in the **Methods** and **Supplementary Information** section (**Supplementary Tables 6 and 7**). For instance, solid-state metathesis reaction of honeycomb layered Na₃Zn_{1.5}TeO₆ precursor with Ca(NO₃)₂·4H₂O at 500 °C for 99 hours in nitrogen atmosphere, yields yafsoanite-type Ca_{1.5}Zn_{1.5}TeO₆ (**Figures 7a,b,c,d,e,f,g,h,i,j,k,l**) Moreover, **Figures 8a,b,c,d,e,f,g,h,I,j,k,l** present high-resolution STEM images of honeycomb-layered Ca_{1.5}Ni₂SbO₆, obtained via a solid-state metathetic reaction involving Ca(NO₃)₂·4H₂O with honeycomb-layered layered Na₃Ni₂SbO₆ (Na₃Ni₂SbO₆ + 1.5Ca(NO₃)₂·4H₂O → Ca_{1.5}Ni₂SbO₆ + 3NaNO₃ + 6H₂O ↑) at 500 °C for 99 hours in nitrogen. The metathesis reaction leads to a topochemical transformation, wherein Na atoms (in octahedral coordination with oxygen) are replaced with Ca atoms (in prismatic coordination with oxygen). In FCC / HCP notation³⁶, the isomorphic topochemical transformation can be expressed as: $U_{\text{O}}V_{(\text{Ni},\text{Ni},\text{Sb})}W_{\text{O}}V_{\text{Na}}U_{\text{O}}V_{(\text{Ni},\text{Ni},\text{Sb})}W_{\text{O}} \text{ etc} \rightarrow U_{\text{O}}V_{(\text{Ni},\text{Ni},\text{Sb})}W_{\text{O}}V_{\text{Ca}}U_{\text{O}}V_{(\text{Ni},\text{Ni},\text{Sb})}W_{\text{O}} \text{ etc.}$, both with Ca coordinated in a prismatic manner to O atoms. Here, the honeycomb arrangement of Ni atoms around Sb is maintained during the topochemical transformation, *modulo* possible finite Burgers vectors and Ni or Ca vacancies. However, due to a transformation from octahedral to prismatic, and the creation of vacancies and other related displacements and distortions in the topochemical transformation, the resultant material is not at all isomorphic to Na₃Ni₂SbO₆, as expected above. In fact, the FCC / HCP notation for the obtained polymorph as is evident in **Figures 8e,f** (*modulo* the Burgers vectors, $\mathbf{b}_- = [\pm 1/6, -1/2, 0]$ and $\mathbf{b}_+ = [\pm 1/6, +1/2, 0]$ implemented respectively by the shear transformations,

$$S_- = \begin{pmatrix} 1 & 0 & \pm 1/6 \\ 0 & 1 & -1/2 \\ 0 & 0 & 1 \end{pmatrix}, S_+ = \begin{pmatrix} 1 & 0 & \pm 1/6 \\ 0 & 1 & +1/2 \\ 0 & 0 & 1 \end{pmatrix}, \quad (2)$$

and neglecting the Ca vacancies) corresponds instead to:

$$W_{\text{O}}U_{(\text{Sb},\text{Ni},\text{Ni})}V_{\text{O}}U_{\text{Ca}}V_{\text{O}}U_{(\text{Ni},\text{Sb},\text{Ni})}W_{\text{O}}U_{\text{Ca}}W_{\text{O}}U_{(\text{Ni},\text{Sb},\text{Ni})}V_{\text{O}}U_{\text{Ca}}V_{\text{O}}U_{(\text{Ni},\text{Sb},\text{Ni})}W_{\text{O}}U_{\text{Ca}}W_{\text{O}}U_{(\text{Ni},\text{Ni},\text{Sb})} \\ V_{\text{O}}U_{\text{Ca}}V_{\text{O}}U_{(\text{Ni},\text{Sb},\text{Ni})}W_{\text{O}}U_{\text{Ca}}W_{\text{O}}U_{(\text{Ni},\text{Sb},\text{Ni})}V_{\text{O}}U_{\text{Ca}}V_{\text{O}}U_{(\text{Ni},\text{Sb},\text{Ni})}W_{\text{O}}U_{\text{Ca}}W_{\text{O}}. \quad (3)$$

Unfortunately, the FCC / HCP notation actually fails to appropriately incorporate local information about the location of the vacancies in the *three* hexagonal sub-lattices given by $U_{\text{Ca}} = U_{(\text{Ca},\text{Ca},\text{Ca})}$ appearing in eq. (3), due to the fact that the hexagonal sub-lattice with any number of vacancies departs from an optimised congruent sphere packing.³⁶

3. Discussion

In employing solid-state metathesis reactions of layered tellurates, we showcase the syntheses of both new and pre-existing Ca- and Mg-based materials, conventionally achievable not only at high temperatures but also under high pressures. For example, the metathetic reaction at temperatures not exceeding 400 °C involving layered Na₄MgTeO₆ with MgCl₂ in ambient pressure (Na₄MgTeO₆ + 2MgCl₂ → Mg₃TeO₆ + 4NaCl) or MgSO₄ under vacuum (Na₄MgTeO₆ + 2MgSO₄ → Mg₃TeO₆ + 2Na₂SO₄) yields the high-pressure, high temperature Mg₃TeO₆ (ilmenite-type) polymorph (**Figures 1a,b,c,d,e,f**), whereas the metathetic reaction involving honeycomb-layered Li₄MgTeO₆ with MgCl₂ (·6H₂O) or MgBr₂·6H₂O produces the ambient pressure, high-temperature Mg₃TeO₆ (corundum-type) polymorph (**Figures 1g,h,i,j,k,l,m,n,o** and **Supplementary Figures 7–9, 49 and 50**). Furthermore, the metathetic reaction of honeycomb-layered Na₂Mg₂TeO₆ with MgCl₂ (at 400 °C) or Mg(NO₃)₂·6H₂O (at 250 °C), yields a metastable Mg₃TeO₆ polymorph (vacancy-type Mg₃TeO₆ (**Figures 2a,b,c,d,e,f,g,h,i,j,k,l**)). The choice of the initial precursor compound (Li₄MgTeO₆, Na₄MgTeO₆, or Na₂Mg₂TeO₆) enables polymorph selectivity of Mg₃TeO₆, with the exothermicity of the byproduct halide/nitrate salts, due to their high lattice energy,^{10,11,16} attributable to favouring the forward reaction. Moreover, the high lattice energy of the byproduct salt along with the low temperatures employed in the metathesis synthetic route confer an advantage in nanoparticle synthesis (**Supplementary Figure 51**), in principle by swiftly arresting growth post-nucleation, preventing substantial crystal growth. This contrasts with traditional solid-state synthesis methods, where high reaction temperatures often result in larger particle sizes owing to processes like particle coarsening and Ostwald ripening during crystal growth.³⁷ Additionally, we extend the solid-state metathetical approach to synthesise Ca-based compounds, such as CaMgSiO₄ (**Supplementary Figure 52**), ilmenite-type CaMg₂TeO₆ (or equivalently as Mg₂CaTeO₆ (**Figures 5a,b,c,d,e,f**), double-perovskite Ca₂MgTeO₆ (**Figures 5g,h,i,j,k,l**), and including their derivative compositions (**Supplementary Tables 6 and 7**). The versatility of the metathetical approach in synthesising a plethora of new Mg- and Ca-based compounds (some of which are exemplified in equation (1)) is extensively detailed in the **Methods** and **Supplementary Information** section.

Figure 9 depicts the crystal structural frameworks of Mg₃TeO₆ polymorphs achieved through solid-state metathesis reactions. The high-pressure, high-temperature Mg₃TeO₆ (ilmenite-type) polymorph framework (crystallising in the acentric *R*3 space group⁵ (**Figures 9b,e**) represents a superstructure of the ambient-pressure, high-temperature Mg₃TeO₆ (corundum-type) polymorph (**Figures 9a,d**), with Mg²⁺ and Te⁶⁺ cations octahedrally coordinated to oxygen ligands. Additionally, the high-pressure, high-temperature Mg₃TeO₆ polymorph exhibits a honeycomb arrangement of TeO₆ and MgO₆ octahedra (**Figure 9e**). One layer is formed by two crystallographically distinct MgO₆ octahedra, whilst the second layer consists of the third MgO₆ octahedra and the TeO₆ octahedra. The alternating sequence of octahedral layers along the *c*-axis, along with two types of layers, results from threefold screw axes (**Supplementary Figure 53**). The ambient-pressure, high-temperature Mg₃TeO₆ (corundum-type) polymorph (crystallising in the centrosymmetric *R* $\bar{3}$ space group²⁹) features centers of inversion symmetry. Structural distinctions arising from the added inversion symmetry centers at the edge centers and corners of the unit cell (viewed along the *c*-axis) are clearly discernible in **Figures 9d,e**. In both crystal structures, the TeO₆ octahedra are separated and not directly connected. The linkage occurs exclusively via MgO₆ octahedra, with six and three edges of the TeO₆ octahedra in the ambient-pressure, high-temperature Mg₃TeO₆ and the high-pressure, high-temperature Mg₃TeO₆ shared with the MgO₆ octahedra, respectively (see also **Supplementary Figure 53**). Vacancy-type Mg₃TeO₆ (ambient-pressure, low-temperature) polymorph exhibits a similar structural motif as the high-pressure, high-temperature Mg₃TeO₆ polymorph when viewed along the *c*-axis (**Figures 9c,f**), featuring distorted MgO₆, MgO₅ and MgO₄ polyhedra coordinated with TeO₆ (**Supplementary Table 8**), resulting in a structure replete with vacancies. Oxide materials featuring five-coordinated MgO₅ polyhedral structures are uncommon; therefore, the vacancy-

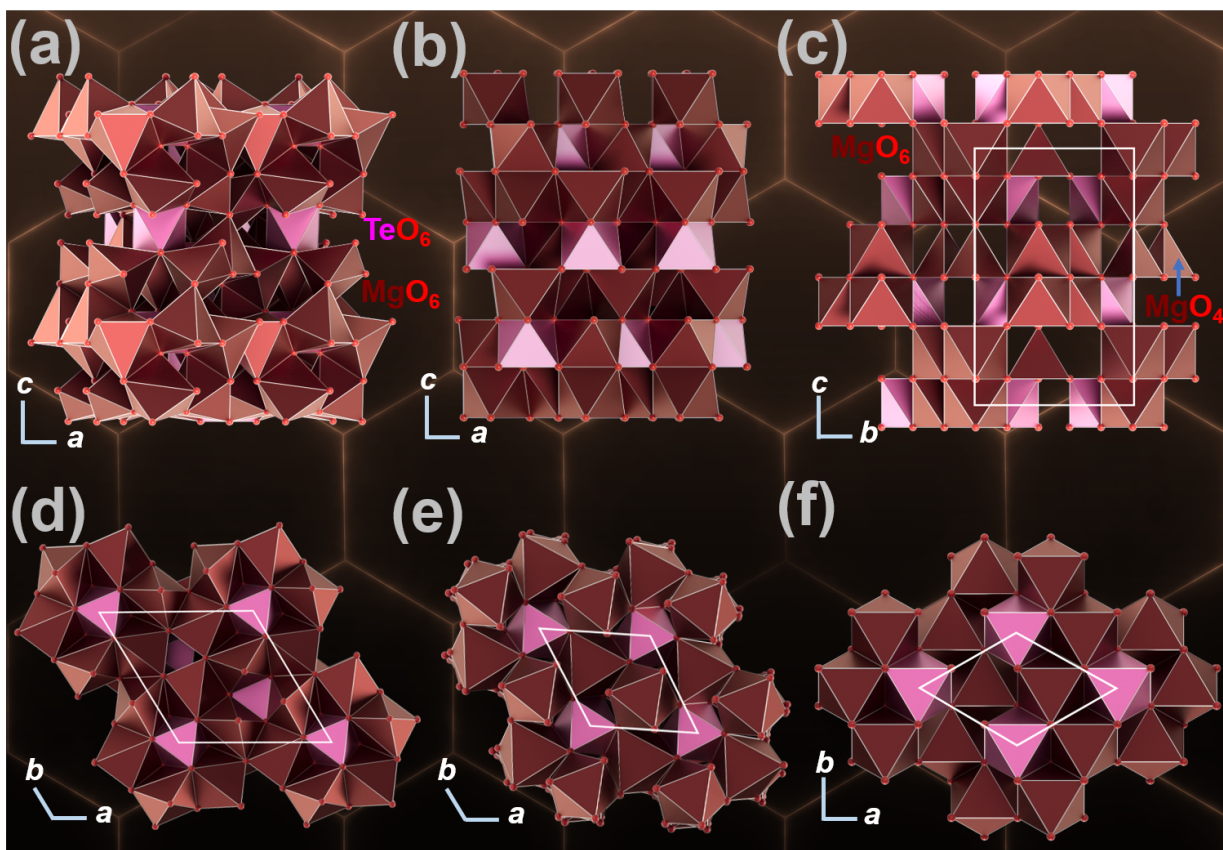


Figure 9 : Mg₃TeO₆ polymorphs. (a) Ambient-pressure, high-temperature Mg₃TeO₆ (corundum-type) polymorph crystal viewed along the [010] zone axis. (b) High-pressure, high-temperature Mg₃TeO₆ (ilmenite-type) polymorph crystal viewed along the [010] zone axis. Mg atom polyhedron (MgO₆ or MgO₄) is shown in brown, whereas Te atom polyhedron (TeO₆) is shown in pink. (c) Vacancy-type (ambient-pressure, low-temperature) Mg₃TeO₆ polymorph crystal viewed along the [100] zone axis. (d) Ambient-pressure, high-temperature Mg₃TeO₆ polymorph crystal viewed along the [001] zone axis. (e) High-pressure, high-temperature Mg₃TeO₆ polymorph crystal viewed along the [001] zone axis. (f) Vacancy-type (ambient-pressure, low-temperature) Mg₃TeO₆ polymorph crystal viewed along the [001] zone axis.

type Mg₃TeO₆ (ambient-pressure, low-temperature polymorph) can be regarded as a metastable phase. With regards to structural considerations and the likelihood of obtaining Mg₃TeO₆ polymorphs (**Supplementary Figure 52**), the stability of Mg₃TeO₆ polymorphs can be inferred to follow the sequence: ambient-pressure, high-temperature Mg₃TeO₆ (corundum-type) > high-pressure, high-temperature Mg₃TeO₆ (ilmenite-type) > vacancy-type (ambient-pressure, low-temperature) Mg₃TeO₆. Structural stability calculations based on density functional theory (**Supplementary Note 1** and **Supplementary Table 9**) further corroborate this hypothesis. Moreover, XRD measurements (**Supplementary Figure 54**) show the vacancy-type Mg₃TeO₆ polymorph to transform to the most stable corundum-type Mg₃TeO₆ polymorph (ambient pressure, high temperature phase) at high temperatures (800°C).

From a technological standpoint, we assessed the viability of employing Mg₃TeO₆ polymorphs as Mg²⁺ conductors. Attenuated total reflection Fourier-transform infrared (ATR-FTIR) and nuclear magnetic resonance (¹H magic-angle spinning (MAS) NMR) measurements on the material powder confirmed the absence of OH⁻ and H⁺ species (**Supplementary Figures 55 and 56**), which could otherwise influence the ionic conductivity of the samples. Whilst the ambient-pressure, high-temperature Mg₃TeO₆ (corundum-type) and vacancy-type Mg₃TeO₆ (ambient pressure, low-temperature) polymorphs display inferior Mg²⁺ conductivity at room temper-

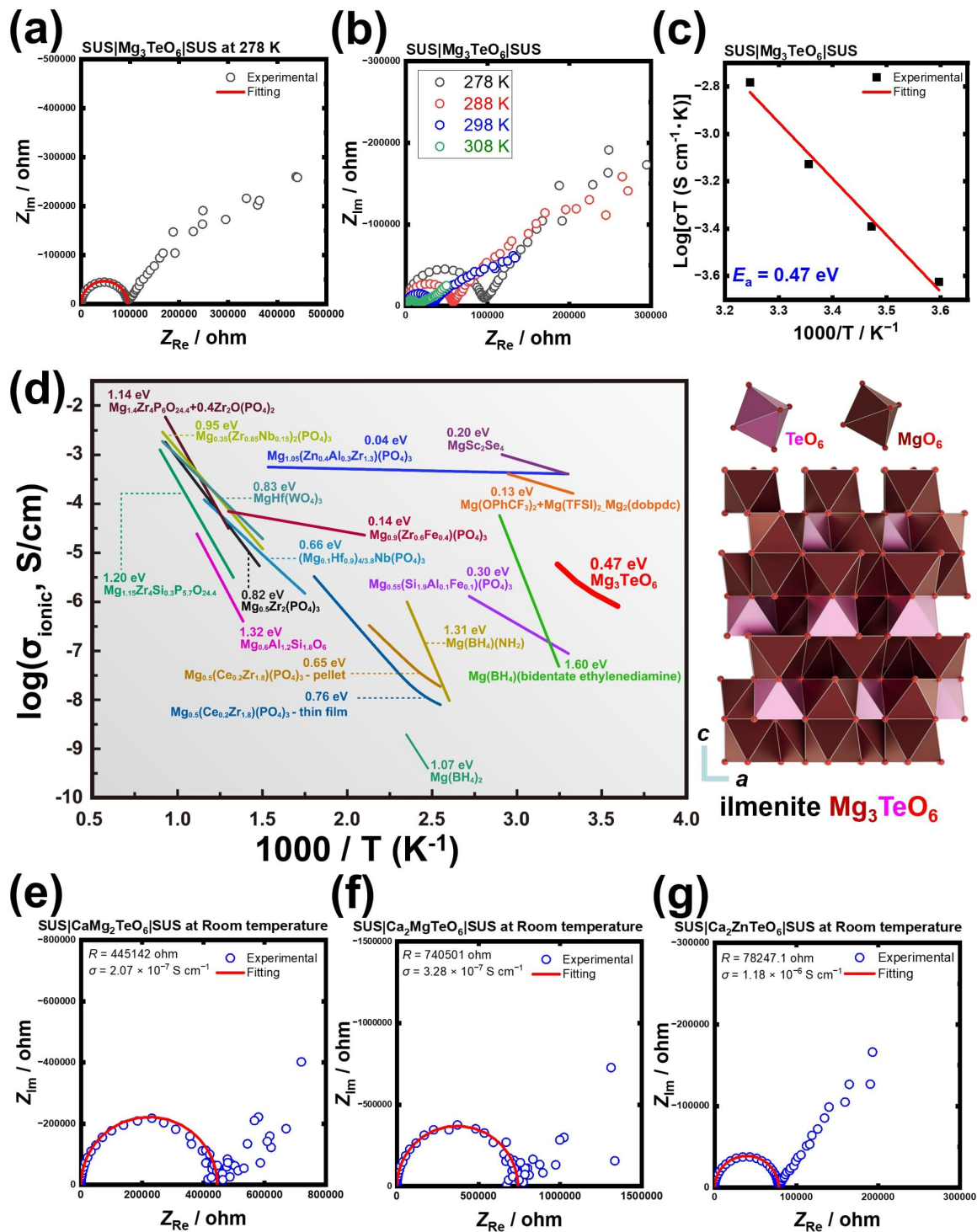
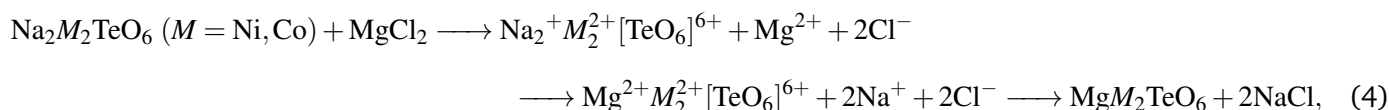


Figure 10 : Electrochemical impedance spectroscopy (EIS) measurements of tellurate-based Mg^{2+} and Ca^{2+} conductors. (a) Nyquist plots taken at 278 K. **(b)** Nyquist plots taken at various temperatures. **(c)** Arrhenius plots derived from EIS measurements of ilmenite-type Mg_3TeO_6 (high pressure, high temperature polymorph) at various temperatures. **(d)** Comparative plots of the ionic conductivity values (σ_{ionic}) against temperature (T) attained in representative Mg-based ionic conductors reported along with the ilmenite-type Mg_3TeO_6 . Details regarding the measurements and synthesis techniques are provided in the **Methods** section. **(e, f, g)** Nyquist impedance plots of $\text{CaMg}_2\text{TeO}_6$ (or equivalently as $\text{Mg}_2\text{CaTeO}_6$), $\text{Ca}_2\text{MgTeO}_6$ and $\text{Ca}_2\text{ZnTeO}_6$ taken at room temperature.

ature (**Supplementary Figure 57**), the high-pressure, high-temperature Mg₃TeO₆ (ilmenite-type) polymorph demonstrates remarkable ionic conductivity (**Figures 10a,b**), despite sub-optimal pellet density. The ionic conductivities of the high-pressure, high-temperature Mg₃TeO₆ polymorph at different temperatures were evaluated, as depicted by the Arrhenius plots in **Figure 10c**. Details regarding the experimental procedures are outlined in the **Methods** section. In the temperature range of 5–45 °C, the high-pressure, high-temperature Mg₃TeO₆ polymorph (with a pellet compactness of ~60 %) exhibited an activation energy of approximately 0.47 eV, calculated by fitting the alternating current data with the Arrhenius equation. The material's ionic conductivity was determined to be $2.5 \times 10^{-6} \text{ S cm}^{-1}$ at 25 °C. Bulk ionic conductivities of the high-pressure, high-temperature Mg₃TeO₆ polymorph are presented for performance benchmarking against reported Mg²⁺ conductors^{38,39} (**Figure 10d**). This figure highlights the potential of the high-pressure, high-temperature Mg₃TeO₆ polymorph as a promising solid electrolyte for all-solid-state magnesium batteries. Further improvements in the ionic conductivity can be anticipated, once the pellet densification process is optimised. Furthermore, we explored the possible use of Ca-based tellurates as Ca²⁺ conductors, considering the scarcity of oxide compounds with appreciable ionic conductivity at room temperature.⁴⁰ **Figures 10e,f,g** depict the electrochemical impedance plots of CaMg₂TeO₆ and double perovskites Ca₂MTeO₆ (*M* = Mg, Zn). Although the possibility of mixed Ca²⁺ and Mg²⁺ conductivity cannot be disregarded in Ca₂MgTeO₆ and CaMg₂TeO₆, double-perovskite Ca₂ZnTeO₆, in particular, exhibits an ionic conductivity of $1.18 \times 10^{-6} \text{ S cm}^{-1}$ at room temperature, primarily arising from Ca²⁺ conduction. This result envisages the broad class of Ca-based double perovskites (*viz.*, Ca₂MTeO₆, Ca_{1.5}M₂RuO₆ and Ca₂MWO₆ (*M* = Mg, Zn, Ca)^{6,28,41–43}), Ca_{1.5}M₂BiO₆ and honeycomb-layered Ca_{1.5}M₂SbO₆ (**Supplementary Tables 6 and 7**), as potential Ca²⁺ conductors in calcium battery solid electrolytes.

The additional advantage of the metathesis reactions involving Li-, Na-, and K-based materials with Ca(NO₃)₂·4H₂O/CaCl₂·2H₂O or MgCl₂/Mg(NO₃)₂·6H₂O/MgSO₄ lies in the spontaneous occurrence of the reactions without the need for pellet compactification to attain Ca-based and Mg-based compounds, as required, for instance, in the preparation of Ca_{*x*}CoO₂ ($0.26 < x \leq 0.50$)⁴⁴. These metathesis reactions initiate spontaneously once the necessary activation energy, E_a is reached. For activation facilitated by changes in the lattice internal energy, the necessary activation energy can be understood via the first law of thermodynamics, $dU = TdS - PdV - \mu dN \equiv E_a$, where $U = TS - PV$ is the internal energy of the unit cell, T is the temperature, S is the entropy, P is the pressure, V is the volume and the Gibbs-Duhem equation, $\mu dN = -SdT + VdP$ with μ the chemical potential and N the total number of *A*-based cations and their vacancies in each unit cell. At constant pressure, particle number and heat energy $\delta Q = TdS$, sufficient activation energy can only be obtained by a net-negative change in the volume of the unit cell. Indeed, this change correlates with a change of the coordination of the *A*-cation from prismatic (*e.g.* Na₂Mg₂TeO₆) to octahedral (vacancy-type Mg₃TeO₆) in the chemical reactions exemplified in eq. (1). On the other hand, vacancy creation and annihilation can be treated as a subset of lattice distortions. Such distortions must increase the entropy of the system ($dS > 0$) injecting disorder into the unit cell. Thus, at constant volume, pressure and temperature, lattice distortions are ideally exothermic ($\delta Q = TdS > 0$), providing additional lattice energy for activation at ambient pressure and considerably lower temperatures. This is the basis of characterising the synthesised materials ridden with such crystalline distortions as high-entropy – a concept reminiscent of nanostructured high-entropy alloys.⁴⁵ Although a precise analysis of the isobaric, isothermal and mechanistic pathway is more intricate and requires computational insights beyond the scope of

the present study, the metathesis reactions detailed herein presumably proceed via an ionic route⁹ *e.g.*,



forming the target material via atomic rearrangements and no change in the oxidation state of the redox-active transition metal atom constituents. Magnetic susceptibility measurements (**Supplementary Figure 57**) indicate that the oxidation states of transition metal atoms remain unaltered after the completion of metathesis reactions *e.g.*, involving Na₂M₂TeO₆ (*M* = Co, Ni) with MgCl₂ to form MgM₂TeO₆ and NaCl end products.

Finally, direct measurement of the maximum temperatures attained in solid-state metathesis reactions proved challenging due to the lack of a reliable thermocouple setup. Nonetheless, the peak temperatures attained in such metathesis reactions are estimated to correlate with the boiling points of the byproduct alkali halide, sulphate, or nitrate salts.¹⁰ Techniques such as remote thermometry offers a promising method for accurately determining these temperatures in metathesis reactions—a subject beyond the scope of the current study.

4. Conclusions

We have demonstrated the expansive applicability of solid-state metathesis reactions, not only in facily accessing known Mg- and Ca-based materials under low temperatures and ambient or vacuum pressures but also in the discovering new materials with potential applications in energy storage. Specifically, through the metathetical approach, we serendipitously synthesised ilmenite-type Mg₃TeO₆ (high-pressure, high-temperature polymorph) at low temperatures and ambient or vacuum pressure, eliminating the need for the megabar pressures conventionally required for its synthesis. Despite the sub-optimal pellet density, this ilmenite-type compound exhibits notable ionic conductivity at room temperature, designating ilmenite-structured materials as promising Mg²⁺ conductors. Furthermore, double-perovskite and garnet compounds incorporating calcium, such as Ca₂ZnTeO₆, display impressive ionic conductivity at room temperature, positioning them as competitive candidates for fast Ca²⁺ conduction. Leveraging the metathesis route, we also synthesised a diverse array of Mg- and Ca-based materials (including silicates, antimonates, ruthenates, and so forth), with potential nanotechnology applications beyond energy storage. A noteworthy aspect of the solid-state metathesis reactions is their adaptability to leverage lithium-, sodium-, and potassium-based functional materials (particularly alkali-rich layered, polyoxyanionic, spinel and rocksalt compounds) for the low-temperature syntheses of calcium- and magnesium-based compounds (**Supplementary Figures 1, 7–12, 49, 50, 52, 59, 60**, and **Supplementary Tables 2–7**), employing cost-effective salt precursors like Ca(NO₃)₂·4H₂O (mineral analogue: nitrocalcite), CaCl₂·2H₂O (sinjarite), MgCl₂ (chloromagnesite), MgSO₄, MgCl₂·6H₂O (bischofite), and Mg(NO₃)₂·6H₂O (nitromagnesite). Future directions for improvement encompass shortening reaction times, presumably through the utilisation of microwave electromagnetic radiation, and optimising the quantity of salt precursors to tailor the nanomorphology of attainable Ca- and Mg-based materials. Finally, the versatility of solid-state metathesis reactions in obtaining new compound classes, characterised by intricate nanocrystal chemistry, offers valuable insights for the development of next-generation functional materials.

5. Methods

5.1. Precursor compounds for metathesis reactions

Precursor compounds, which entailed lithium-, sodium-, potassium- and silver-based compounds, were prepared either by the conventional solid-state reaction synthesis route or the topochemical ion-exchange route, as detailed elsewhere^{2,46} **Supplementary Table 10** summarises the synthetic conditions used to attain various precursors.

5.2. Metathesis reactions involving Ca salts

Unless otherwise stated, all protocols detailed herein were performed in a super dry room with a dew point maintained below -75°C dP. Metathesis reactions to synthesise calcium-based compounds were conducted using nitrocalcite ($\text{Ca}(\text{NO}_3)_2 \cdot 4\text{H}_2\text{O}$; Sigma Aldrich, 99.0%) or $\text{CaCl}_2 \cdot 2\text{H}_2\text{O}$ (Kishida Chemicals, 99%) at 500°C under a nitrogen atmosphere. The heating temperature was determined based on (i) thermogravimetric measurements of the calcium salts (**Supplementary Figure 61**), indicating the temperature regime at which they are stable, and (ii) X-ray diffraction measurements of the reactions at various temperatures, indicating the temperature and duration (dwell time) necessary to trigger a complete metathesis reaction.

The precursors (Li-, Na-, K-, or Ag-based compounds) were intimately mixed with $\text{Ca}(\text{NO}_3)_2 \cdot 4\text{H}_2\text{O}$ or $\text{CaCl}_2 \cdot 2\text{H}_2\text{O}$ using an agate mortar and pestle, and then placed in a gold or platinum crucible. Alumina crucibles could also be used, *albeit* posing some challenge in removing some fired powders that adhered to the bottom of the alumina crucibles. The mixture was heated at 500°C in a fixed nitrogen flux for 99 hours. The heating furnace was equipped with a fractional distillation system (Full-Tech, FT-N2-SP) that automatically supplied a constant nitrogen flux maintained at 1 L min^{-1} .

For instance, $\text{Ca}_2\text{MgTeO}_6$ can be prepared via the following metathesis reaction using Ca salt at 500°C in a fixed nitrogen flux for 99 hours (**Supplementary Figure 62**):



A slight molar excess (10% mol) of $\text{Ca}(\text{NO}_3)_2 \cdot 4\text{H}_2\text{O}$ was utilised to ensure complete metathesis reaction. As for solid-state metathesis reactions involving $\text{CaCl}_2 \cdot 2\text{H}_2\text{O}$, a two-fold molar excess of $\text{CaCl}_2 \cdot 2\text{H}_2\text{O}$ was used. The resulting products, after completion of the metathesis reactions, were washed with ethanol (Kishida Chemicals, 99.5%) under magnetic stirring to dissolve the remaining $\text{Ca}(\text{NO}_3)_2 \cdot 4\text{H}_2\text{O}$ and byproduct salts (*e.g.*, LiNO_3 , NaNO_3 , *etc.*). Methanol could also be used, although we restricted ourselves to using ethanol due to the hazardous effects of handling methanol. It should also be noted that metathesis reactions involving K-based compound precursors with $\text{Ca}(\text{NO}_3)_2 \cdot 4\text{H}_2\text{O}$ yield KNO_3 as a byproduct, which is slightly soluble in ethanol. In this case, glycerol or distilled water could be used to completely dissolve the nitrate byproduct salt. Note that distilled water can only be used for metathesis reactions in which the target compounds are not hygroscopic. Thus, the choice of solvent depends on (i) the solubility of the byproduct (*i.e.*, alkali nitrates, chlorides, *etc.* (**Supplementary Table 11**)), (ii) the solubility of $\text{Ca}(\text{NO}_3)_2 \cdot 4\text{H}_2\text{O}$ or $\text{CaCl}_2 \cdot 2\text{H}_2\text{O}$ (**Supplementary Table 12**) and (iii) the hygroscopicity of the target compounds. The target compound was finally washed with acetone, prior to drying for 10 hours in a vacuum oven at 100°C .

When the metathesis reaction (exemplified in equation (5)) was conducted at 500°C in air, instead of

nitrogen, CaCO₃ (vaterite) was observed as a minor impurity phase (**Supplementary Figure 63**). In addition to using Ca(NO₃)₂·4H₂O, limited experiments were also performed with CaCl₂·2H₂O (Kishida Chemicals, 99%), CaCl₂ (Fujifilm Wako Pure Chemicals), and CaBr₂ (Tokyo Chemical Industry (TCI), 97%) (**Supplementary Figure 64**), indicating that hydrated calcium salts are effective for synthesising calcium-based compounds via such metathesis reactions.

Metathesis reactions of Ag-based compounds with Ca(NO₃)₂·4H₂O or CaCl₂·2H₂O at 500 °C yielded the target compound along with Ag metal as a byproduct (**Supplementary Figure 65**). This occurs because the AgNO₃ byproduct, in principle, decomposes to Ag according to the following reaction:



Each typical batch yielded approximately 0.5 g of the target product. To increase the sample quantity, up to 10 batches were occasionally fired together in a single furnace session, resulting in a total yield of 5 g. Notably, depending on furnace capacity, metathesis reactions can be further optimised to produce larger quantities of the target powder on a pilot scale. A summary of the metathesis synthesis protocol for Ca-based compounds is illustrated in **Supplementary Figure 66**.

5.3. Metathesis reactions involving Mg salts

Metathesis reactions to attain Mg-based compounds were also performed in a super dry room with a dew point maintained below -75°C dP. Nitromagnesite (Mg(NO₃)₂·6H₂O (Kishida Chemicals)) and chloromagnesite (MgCl₂ (Sigma-Aldrich, >98%)) were mainly used in the metathesis reactions involving Li-, Na-, K-, or Ag-based compound precursors.

For instance, Mg₃TeO₆ can be prepared via the following metathesis reaction at 250°C in air or nitrogen atmosphere for 99 hours:



A twofold molar excess of Mg(NO₃)₂·6H₂O was utilised to ensure complete reaction. The precursors (Li-, Na-, K-, or Ag-based compounds) were intimately mixed with Mg(NO₃)₂·6H₂O using an agate mortar and pestle, and then placed in a gold, platinum or alumina crucibles. The resulting products, after completion of the metathesis reactions (at 250°C in N₂ for 99 hours), were washed with distilled water under magnetic stirring to dissolve the remaining Mg(NO₃)₂·6H₂O and byproduct nitrate salts (*e.g.*, NaNO₃). The choice of solvent depends on (i) the solubility of the byproduct (*i.e.*, alkali nitrates, chlorides, *etc.* (**Supplementary Table 11**)) and (ii) the solubility of Mg salt initially used (**Supplementary Table 13**). The target compound was finally washed with acetone, prior to drying for 10 hours in a vacuum oven at 100°C. Subsequently, the target compound was reannealed at 400°C for 24 hours under a nitrogen atmosphere (depending on the initial crystallinity) to enhance the material's crystallinity.

Metathesis reactions involving MgCl₂ were performed at 400°C for 99 hours under nitrogen or air. Just as is the case for metathesis reactions involving Ca salts, the heating temperature for metathesis reactions entailing Mg salts (MgBr₂ (Fujifilm Wako Pure Chemicals), MgCl₂ (Sigma-Aldrich, >98%), MgBr₂·6H₂O (Fujifilm Wako Pure Chemicals, 99.9%), MgSO₄·7H₂O (Kishida Chemicals, 99.5%), MgCl₂·6H₂O (Kishida Chemicals, 98%), MgSO₄ (Kishida Chemicals)) was determined based on (i) thermogravimetric measurements of the magnesium salts (**Supplementary Figure 67**), indicating the temperature regime at which they are stable, and (ii) X-

ray diffraction measurements of the reactions at various temperatures (**Supplementary Figures 68 and 69**), indicating the temperature and duration (dwell time) necessary to trigger the complete metathesis reactions.

Metathesis reactions to yield Mg-based compounds were found to be contingent on the firing atmosphere, precursors and Mg salts used, with some reactions (particularly those involving MgCl₂) yielding trace to significant amounts of MgO (**Supplementary Figure 59a**). A summary of the metathesis protocol is illustrated in **Supplementary Figure 70**.

Additionally, for the sake of comparison, powder samples of MgM₂TeO₆ (*M* = Co, Cu, Ni, Zn, Mg), Mg₂MTeO₆, and Mg_{1.5}M_{1.5}TeO₆ were also prepared using high-temperature solid-state ceramics route (**Supplementary Figure 41**). **Supplementary Tables 1 and 2** show the annealing conditions utilised to attain Mg-based samples.

5.4. X-ray diffraction (XRD) analyses

Conventional XRD analyses were undertaken utilising a Bruker D8 ADVANCE diffractometer to elucidate the crystallinity of both the precursors and the powder samples attained via solid-state metathesis reactions. The measurements were executed in Bragg-Brentano geometry mode employing Cu-K α radiation. Rietveld analyses were conducted for compounds from which meaningful structural data could be extracted (**Supplementary Figures 50 and 52**).

5.5. Morphological and physicochemical characterisation

The chemical composition of the compounds attained via metathesis reactions were analysed by a scanning electron microscope (JSM-6510LA) carried out using the energy dispersive X-ray (EDX) imaging function. Stoichiometry quantifications, particularly of Ca-based compounds, were precisely determined by inductively coupled plasma mass spectrometry (ICP-MS). High-resolution scanning TEM (STEM) imaging was executed utilising a JEOL JEM-ARM200F, equipped with a CEOS CESCOR STEM Cs corrector (spherical aberration corrector), under an acceleration voltage set at 200 kV. STEM images for CaMg₂TeO₆, Ca₂MgTeO₆ (**Figure 5**) and Ca_{1.5}Ni₂SbO₆ (**Figure 8**) were acquired using a JEM-ARM200F (NEOARM), equipped with a CEOS ASCOR Cs corrector. Details pertaining to the sample preparation, are as detailed in ref. 47. Electron microscopy measurements were systematically performed along various zone axes, specifically [100], [110], and [310] zone axes.

5.6. Ionic conductivity measurements

Powder samples of MgM₂TeO₆, Mg₂MTeO₆, CaM₂TeO₆, and Ca₂MTeO₆ (*M* = Mg, Zn, Ca) underwent uniaxial pressing to form pellets with 10 mm diameters, applying a pressure of approximately 40 MPa. Stainless steel (SUS) served as the current collector for these pellets, with densities reaching around 50~60% of their respective theoretical ceramic densities. Electrochemical impedance measurements (**Figures 10a,b,e,f,g** and **Supplementary Figure 57**) were conducted based on the protocols detailed elsewhere⁴⁷, with careful measures taken to avoid exposing samples to moisture in the air.

The activation energy (*E_a*) for magnesium-ion or calcium-ion conduction was determined through linear fitting of bulk ionic conductivity values at different temperatures, employing the well-established Arrhenius equation as detailed in ref. 47. EC-Lab software package Z-fit was used to fit all equivalent circuits of the Nyquist plots.

5.7. Magnetic susceptibility measurements

To assess the valency state of the transition metal atoms in the as-prepared MgM₂TeO₆ (*M* = Co, Ni) samples, magnetic susceptibility measurements (**Supplementary Figure 58**) were performed using a Quantum Design Magnetic Property Measurement System, at a temperature range of 2–300 K and a magnetic field range of ± 70

kOe.

5.8. Attenuated total reflectance Fourier-transform infrared spectroscopy (ATR-FTIR) measurements

ATR-FTIR spectra were obtained using an IRTracer-100 FTIR spectrometer (Shimadzu, Japan) equipped with a single-reflection ATR accessory featuring a diamond crystal (QATR 10). For each sample, 512 scans were averaged over the range of 4000 to 400 cm⁻¹ with a resolution of 4 cm⁻¹. Background scans were conducted prior to spectrum acquisition. The presence or absence of H₂O in the target samples was determined by analysing the characteristic absorption peaks observed in the ATR-FTIR spectra. Calcium- and magnesium-based compounds synthesised via solid-state metathesis reactions were subjected to ATR-FTIR analysis to detect any traces of H₂O (**Supplementary Figure 56**). These analyses were benchmarked against reference compounds such as Mg(NO₃)₂·6H₂O, H₆TeO₆ (or equivalently as Te(OH)₆), and H₂Mg₂TeO₆. The H₂Mg₂TeO₆ reference compound was synthesised through protonation of Na₂Mg₂TeO₆ using 2 M acetic acid (CH₃COOH), based on the following reaction: Na₂Mg₂TeO₆ + 2CH₃COOH → 2CH₃COONa + H₂Mg₂TeO₆. The absence of spectral features corresponding to H₂O (-OH functional groups) in the compounds obtained via solid-state metathesis reactions suggests that neither H⁺ nor OH⁻ ions were present, ensuring that the ionic conductivity measurements were not influenced by these species (*i.e.*, H⁺, OH⁻).

5.9. Nuclear magnetic resonance (NMR) measurements

¹H magic-angle spinning (MAS) NMR measurements (**Supplementary Figure 55**) were conducted at 298 K using a Bruker AV-300 spectrometer, operating at a ¹H Larmor frequency of 300 MHz, with a 1.4 mm MAS probe at a 40 kHz spinning speed. Spectra acquisition employed a rotor-synchronised Hahn echo sequence (90° - τ - 180° - τ - acquisition), and signal intensities were normalised based on the sample weights within the rotors. A recycle delay of 10 s was used to collect a total of 256 scans for each sample. ¹H chemical shifts were referenced to the CH₃COOLi resonance at -1.27 ppm.

5.10. Thermogravimetric measurements

Thermogravimetric and differential thermal analysis (TG-DTA) were performed using a Bruker AXS 2020SA TG-DTA instrument in either nitrogen or air atmosphere. The samples were briefly exposed to air whilst being loaded into platinum crucibles prior to measurement. The analysis (**Supplementary Figures 61 and 67**) was conducted over a temperature range between 25 and 1000 °C, at a heating rate of 5 °C min⁻¹.

5.11. Computational details

Density functional theory (DFT) calculations were employed to evaluate the structural stability of the Mg₃TeO₆ polymorphs, following the computational formalism outlined in previous studies.⁴⁸ Additional information regarding the methodology and parameters used is available in **Supplementary Note 1**.

Supplementary Information

The online link to the Supplementary Information, which includes additional experimental details, will be made available in future updates of the preprint.

Acknowledgements

This work was supported by Green Technologies for Excellence (GteX) Program of the Japan Science and Technology Agency (JST). T.M. and G.M.K. would like to acknowledge the financial support from AIST Edge Runners Funding. G.M.K. gratefully acknowledges the Japan Society for the Promotion of Science (JSPS) for the support of his fellowship. S.K. acknowledges funding from the JST FOREST Grant (No. JPMJFR212V). The computations in this work were conducted using the facilities of the Supercomputer Center at the Institute for Solid State Physics, University of Tokyo.

Conflicts of interest

There are no conflicts to declare.

References

- 1 G. M. Kanyolo, T. Masese, Y. Miyazaki, S. Tachibana, C. Zhong, Y. Oriksa and T. Saito, *Progress in Materials Science*, 2023, 101205.
- 2 G. M. Kanyolo, T. He, A. Alshehabi and Z.-D. Huang, *Materials Today Chemistry*, 2023, **33**, 101657.
- 3 G. M. Kanyolo, T. Masese, N. Matsubara, C.-Y. Chen, J. Rizell, Z.-D. Huang, Y. Sassa, M. Månsson, H. Senoh and H. Matsumoto, *Chemical Society Reviews*, 2021, **50**, 3990–4030.
- 4 G. M. Kanyolo and T. Masese, *Materials Today Physics*, 2023, **39**, 101271.
- 5 E. Selb, L. Declara, L. Bayarjargal, M. Podewitz, M. Tribus and G. Heymann, *European Journal of Inorganic Chemistry*, 2019, **2019**, 4668–4676.
- 6 H.-G. Burckhardt, C. Platte and M. Trömel, *Acta Crystallographica Section B: Structural Crystallography and Crystal Chemistry*, 1982, **38**, 2450–2452.
- 7 M. E. Arroyo-de Dompablo, A. Ponrouch, P. Johansson and M. R. Palacín, *Chemical Reviews*, 2019, **120**, 6331–6357.
- 8 P. Saha, M. K. Datta, O. I. Velikokhatnyi, A. Manivannan, D. Alman and P. N. Kumta, *Progress in Materials Science*, 2014, **66**, 1–86.
- 9 R. E. Treece, J. A. Conklin and R. B. Kaner, *Inorganic Chemistry*, 1994, **33**, 5701–5707.
- 10 I. Parkin, *Chemical Society Reviews*, 1996, **25**, 199–207.
- 11 A. M. Nartowski, I. P. Parkin, A. J. Craven and M. MacKenzie, *Advanced Materials*, 1998, **10**, 805–808.
- 12 N. Ugemuge, D. Tajne, S. Dhopte, P. Muthal and S. Moharil, *Physica B: Condensed Matter*, 2011, **406**, 45–47.
- 13 E. G. Gillan and R. B. Kaner, *Inorganic Chemistry*, 1994, **33**, 5693–5700.
- 14 R. F. Jarvis, R. M. Jacobinas and R. B. Kaner, *Inorganic Chemistry*, 2000, **39**, 3243–3246.
- 15 A. Miura, H. Ito, C. J. Bartel, W. Sun, N. C. Rosero-Navarro, K. Tadanaga, H. Nakata, K. Maeda and G. Ceder, *Materials Horizons*, 2020, **7**, 1310–1316.
- 16 P. R. Bonneau, R. F. Jarvis Jr and R. B. Kaner, *Inorganic Chemistry*, 1992, **31**, 2127–2132.
- 17 A. J. Martinolich, J. A. Kurzman and J. R. Neilson, *Journal of the American Chemical Society*, 2016, **138**, 11031–11037.
- 18 T. K. Mandal and J. Gopalakrishnan, *Journal of Materials Chemistry*, 2004, **14**, 1273–1280.
- 19 T. K. Mandal and J. Gopalakrishnan, *Chemistry of Materials*, 2005, **17**, 2310–2316.
- 20 J. Gopalakrishnan, T. Sivakumar, K. Ramesha, V. Thangadurai and G. Subbanna, *Journal of the American Chemical Society*, 2000, **122**, 6237–6241.
- 21 Y. Haraguchi, C. Michioka, A. Matsuo, K. Kindo, H. Ueda and K. Yoshimura, *Physical Review Materials*, 2018, **2**, 054411.

- 22 Y. Haraguchi, K. Nawa, C. Michioka, H. Ueda, A. Matsuo, K. Kindo, M. Avdeev, T. J. Sato and K. Yoshimura, *Physical Review Materials*, 2019, **3**, 124406.
- 23 T. Sivakumar, K. Ramesha, S. Lofland, K. Ramanujachary, G. Subbanna and J. Gopalakrishnan, *Inorganic Chemistry*, 2004, **43**, 1857–1864.
- 24 P. Parhi, V. Manivannan, S. Kohli and P. McCURDY, *Bulletin of Materials Science*, 2008, **31**, 885–890.
- 25 P. Parhi and V. Manivannan, *Journal of Alloys and Compounds*, 2009, **469**, 558–564.
- 26 J. W. Kramer, S. A. Isaacs and V. Manivannan, *Journal of Materials Science*, 2009, **44**, 3387–3392.
- 27 P. Parhi and V. Manivannan, *Solid State Sciences*, 2008, **10**, 1012–1019.
- 28 Y. J. Shan, Y. Kanai, K. Tezuka and H. Imoto, *Advances in Science and Technology*, 2006, **45**, 2572–2575.
- 29 A. Bhim, J. Gopalakrishnan and S. Natarajan, *European Journal of Inorganic Chemistry*, 2018, **2018**, 2277–2284.
- 30 M. Evstigneeva, V. Nalbandyan, A. Petrenko, B. Medvedev and A. A. Kataev, *Chemistry Of Materials*, 2011, **23**, 1174–1181.
- 31 B. Klaassen, *European Journal of Combinatorics*, 2022, **100**, 103454.
- 32 R. D. Shannon, *Acta crystallographica section A: crystal physics, diffraction, theoretical and general crystallography*, 1976, **32**, 751–767.
- 33 L. Xiao, Z. Ding, C. Chen, Z. Han, P. Wang, Q. Huang, P. Gao and W. Wei, *Iscience*, 2020, **23**, 100898.
- 34 P. M. Woodward, *Acta Crystallographica Section B: Structural Science*, 1997, **53**, 32–43.
- 35 D. Jarosch and J. Zemmann, *Mineralogy and Petrology*, 1989, **40**, 111–116.
- 36 G. M. Kanyolo and T. Masese, *Advances in honeycomb layered oxides: Part II–Theoretical advances in the characterisation of honeycomb layered oxides with optimised lattices of cations*, 2022.
- 37 P. W. Voorhees, *Journal of Statistical Physics*, 1985, **38**, 231–252.
- 38 P. W. Jaschin, Y. Gao, Y. Li and S.-H. Bo, *Journal of Materials Chemistry A*, 2020, **8**, 2875–2897.
- 39 M. Guo, C. Yuan, T. Zhang and X. Yu, *Small*, 2022, **18**, 2106981.
- 40 S. S. Shinde, N. K. Wagh, S.-H. Kim and J.-H. Lee, *Advanced Science*, 2023, **10**, 2304235.
- 41 G. Blasse, *Journal of Inorganic and Nuclear Chemistry*, 1965, **27**, 993–1003.
- 42 S. Patwe, S. Achary, M. Mathews and A. Tyagi, *Materials Chemistry and Physics*, 2006, **98**, 486–493.
- 43 J. Baglio and S. Natansohn, *Journal of Applied Crystallography*, 1969, **2**, 252–254.
- 44 B. L. Cushing and J. B. Wiley, *Journal of Solid State Chemistry*, 1998, **141**, 385–391.
- 45 J.-W. Yeh, S.-K. Chen, S.-J. Lin, J.-Y. Gan, T.-S. Chin, T.-T. Shun, C.-H. Tsau and S.-Y. Chang, *Advanced engineering materials*, 2004, **6**, 299–303.

- 46 Z. He, W. Guo, M. Cui and Y. Tang, *Dalton Transactions*, 2017, **46**, 5076–5081.
- 47 T. Masese, G. M. Kanyolo, Y. Miyazaki, M. Ito, N. Taguchi, J. Rizell, S. Tachibana, K. Tada, Z.-D. Huang, A. Alshehabi *et al.*, *Advanced Science*, 2022, 2204672.
- 48 K. Tada, T. Masese and G. M. Kanyolo, *Computational Materials Science*, 2022, **207**, 111322.